PLOS COMPUTATIONAL BIOLOGY

RESEARCH ARTICLE

Binding free energy decomposition and multiple unbinding paths of buried ligands in a $PreQ_1$ riboswitch

Guodong Hu[1,2], **Huan-Xiang Zhou**[2,3]*

1 Shandong Key Laboratory of Biophysics, Dezhou University, Dezhou, China, **2** Department of Chemistry, University of Illinois at Chicago, Chicago, Illinois, United States of America, **3** Department of Physics, University of Illinois at Chicago, Chicago, Illinois, United States of America

* hzhou43@uic.edu

Citation: Hu G, Zhou H-X (2021) Binding free energy decomposition and multiple unbinding paths of buried ligands in a $PreQ_1$ riboswitch. PLoS Comput Biol 17(11): e1009603. https://doi.org/10.1371/journal.pcbi.1009603

Editor: Shi-Jie Chen, University of Missouri, UNITED STATES

Received: July 20, 2021

Accepted: October 31, 2021

Published: November 12, 2021

Peer Review History: PLOS recognizes the benefits of transparency in the peer review process; therefore, we enable the publication of all of the content of peer review and author responses alongside final, published articles. The editorial history of this article is available here: https://doi.org/10.1371/journal.pcbi.1009603

Data Availability Statement: DATA AVAILABILITY Structures from molecular dynamics simulations and data files presented as plots in figures are available on GitHub at: https://github.com/hzhou43/PreQ1_Riboswitch.

Abstract

Riboswitches are naturally occurring RNA elements that control bacterial gene expression by binding to specific small molecules. They serve as important models for RNA-small molecule recognition and have also become a novel class of targets for developing antibiotics. Here, we carried out conventional and enhanced-sampling molecular dynamics (MD) simulations, totaling 153.5 μs, to characterize the determinants of binding free energies and unbinding paths for the cognate and synthetic ligands of a $PreQ_1$ riboswitch. Binding free energy analysis showed that two triplets of nucleotides, U6-C15-A29 and G5-G11-C16, contribute the most to the binding of the cognate ligands, by hydrogen bonding and by base stacking, respectively. Mg^{2+} ions are essential in stabilizing the binding pocket. For the synthetic ligands, the hydrogen-bonding contributions of the U6-C15-A29 triplet are significantly compromised, and the bound state resembles the apo state in several respects, including the disengagement of the C15-A14-A13 and A32-G33 base stacks. The bulkier synthetic ligands lead to significantly loosening of the binding pocket, including extrusion of the C15 nucleobase and a widening of the C15-C30 groove. Enhanced-sampling simulations further revealed that the cognate and synthetic ligands unbind in almost opposite directions. Our work offers new insight for designing riboswitch ligands.

Author summary

Riboswitches are bacterial RNA elements that change structures upon binding a cognate ligand. They are of great interest not only for understanding gene regulation but also as targets for designing small-molecule antibiotics and chemical tools. Understanding the molecular determinants for ligand affinity and selectivity is thus crucial for designing synthetic ligands. Here we carried out extensive molecular dynamics simulations of a $PreQ_1$ riboswitch bound to either cognate or synthetic ligands. By comparing and contrasting these two groups of ligands, we learn how the chemical (e.g., number of hydrogen bond donors and acceptors) and physical (e.g., molecular size) features of ligands affect binding affinity and ligand exit paths. While the number of hydrogen bond donors and acceptors

Funding: This work was supported by National Institutes of Health Grant GM118091 (to HXZ). GH's participation in this work was also partially supported by Natural Science Foundation of Shandong Province Grant ZR2019MA040 and National Natural Science Foundation of China Grant 62071085. The funders had no role in study design, data collection and analysis, decision to publish, or preparation of the manuscript.

Competing interests: The authors have declared that no competing interests exist.

is a key determinant for RNA binding affinity, the ligand size affects the rigidity of the binding pocket and thereby regulates the unbinding of the ligand. These lessons provide guidance for designing riboswitch ligands.

Introduction

Noncoding RNAs mediate essential cellular processes such as gene expression and their dysregulation is linked to infectious diseases and cancer [1,2]. They can fold into intricate three-dimensional structures with pockets that potentially serve as binding sites for small molecules [3,4]. There is growing interest in developing RNA-binding small molecules as therapeutics and chemical probes [5,6]. Riboswitches are structured non-coding RNA elements that occur in 5′ untranslated regions of mRNA, most often in bacteria [7]. A riboswitch typically consists of two domains: a conserved aptamer domain that folds into a structure with a binding pocket for a ligand molecule, and an expression platform that interfaces with the transcriptional or translational machinery. Directed by the presence or absence of the ligand, the two domains compete for a switch sequence, resulting in two alternative structures for the expression platform that correspond to the on and off states of the mRNA. Ligands range from nucleobases, cofactors, and amino acids to metal ions [8–15]. Riboswitches bind their cognate ligands with high affinity and high selectivity. These important properties make riboswitches prime targets for developing small-molecule antibiotics and chemical tools [16–23].

The smallest known aptamer domain is from the class 1 $PreQ_1$ riboswitch. With 33 nucleotides, this aptamer forms a compact H-type pseudoknot when bound with $PreQ_1$ [24,25] (Fig 1A). The structure consists of two stems: A-form stem S1 formed by pairing the C1 to G5 bases with the G20 to C16 bases, and pseudoknotted stem S2 with canonical C30-G11 and G33-C9 pairs flanking noncanonical A31-G8 and A32-A10 pairs. The intervening sequences are called loops L1 (U6 to C7), L2 (U12 to C15), and L3 (U21 to A29). Prequeuosine0 ($PreQ_0$, or Q_0 for short) and prequeuosine1 ($PreQ_1$, or Q_1 for short) are precursors (Fig 1B) to the modified guanine nucleotide queuosine. $PreQ_1$ and $PreQ_0$ have a modest difference in binding affinity (with K_D at 2.05 ± 0.29 nM and 35.10 ± 6.07 nM, respectively) for the aptamer from *Thermoanaerobacter tengcongensis* (*Tte*) [24]. Their crystal structures show very similar poses [24–26]. $PreQ_1$ forms in-plane hydrogen bonds with U6, C15, and A29, and stacks against G5 and C16 on one side and against G11 on the other side (Fig 1A). In the crystal structure of the apo form, the *Tte* aptamer assumes the same fold, but loop L2 in particular is reorganized, with the A14 base inserted into the $PreQ_1$-binding pocket whereas the C15 base extruded from the core. Also worth noting are several Mn^{2+} ions (mimicking Mg^{2+}) resolved in the latest crystal structure of the $PreQ_1$-bound (or apo) *Tte* aptamer [25]. The structures of the *Tte* aptamer bound with three synthetic ligands (L_1 to L_3; Fig 1C), but with the A13 and A14 (or even C15) nucleobases removed, have been determined [23]. The synthetic ligands are bulkier than $PreQ_1$, and their binding affinities for the *Tte* aptamer were 50 to 300-fold lower. In the crystal structures, the synthetic ligands, like $PreQ_1$ and $PreQ_0$, are sandwiched between G5 and C16 on one side and G11 on the other side, but within the ligand plane, only A29 forms a hydrogen bond with the ligands. The reduced number of hydrogen bonds may explain the weaker affinities, but the removal of the L2 nucleobases in the crystal structures complicates the interpretation.

More importantly, crystal structures provide only a single snapshot from an ensemble of conformations. Additional information, in particular energetic and dynamic properties, can come from molecular dynamics (MD) simulations. For example, MD simulations have been

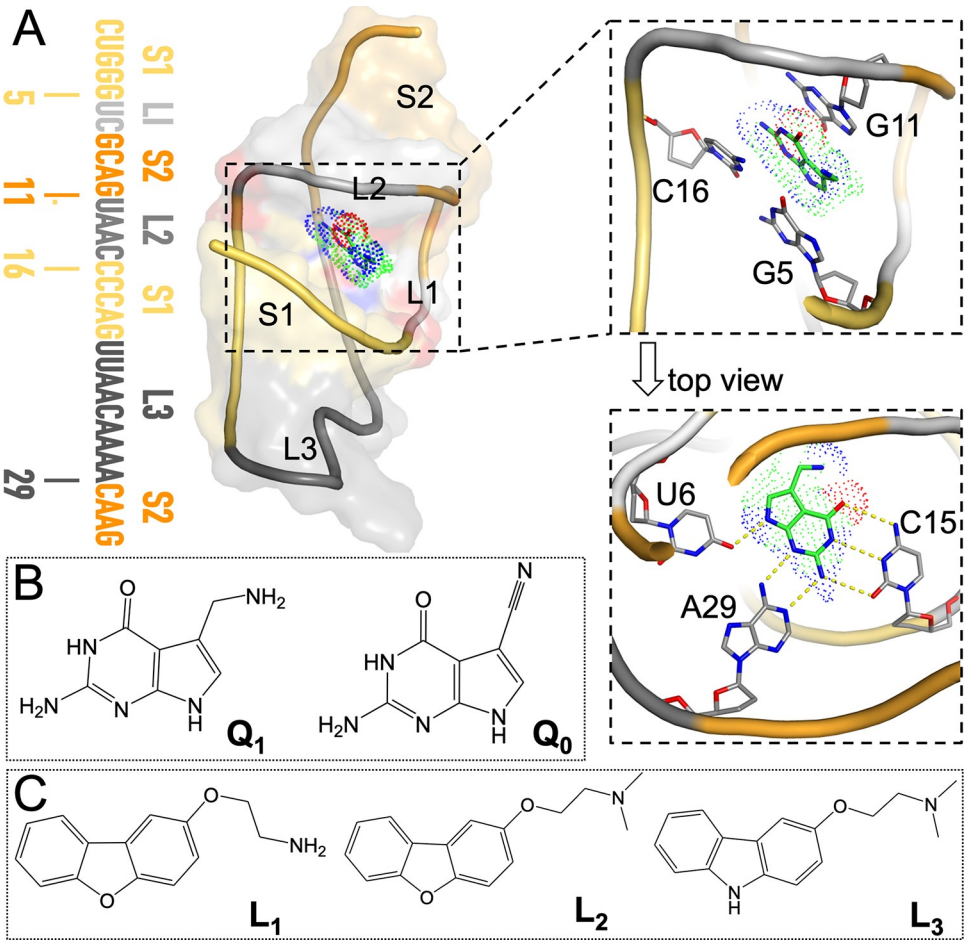

Fig 1. Structures of the $PreQ_1$-bound aptamer domain from the *Tte* $PreQ_1$ riboswitch and of the cognate and synthetic ligands. (A) Left: sequence and secondary structure of the aptamer; middle: three-dimensional structure of the $PreQ_1$-aptamer complex, with the aptamer shown in both cartoon and surface representations. Nucleotides in the sequence and in the structure are color-matched. Top right: zoomed version showing $PreQ_1$ in an oblique view to highlight the base stacking with G11 above and with G5 and C16 below. Bottom right: top view highlighting the in-plane hydrogen bonding with U6, C15, and A29. This structure was prepared using coordinates from the PDB entry 6E1W [23], with missing nucleotides copied from PDB entry 3Q50 [24]. (B) Chemical structures of $PreQ_1$ and $PreQ_0$. (C) Chemical structures of three synthetic ligands, L_1 to L_3.

https://doi.org/10.1371/journal.pcbi.1009603.g001

used to investigate ligand-induced conformational changes of the aptamer domains from the guanine, adenine, and S-adenosylmethionine sensing riboswitches [27–30]. The small size of the $PreQ_1$ riboswitch aptamer makes it attractive for MD simulations [31–33]. Questions regarding binding affinity and selectivity can be addressed by binding free energy calculations, such as by the molecular mechanics Poisson-Boltzmann surface area (MM-PBSA) method [34]. A detailed description of the ligand binding and unbinding paths provide additional insight. As ligand entrance to and exit from a buried site, as found in the $PreQ_1$ riboswitch, occur in timescales usually beyond the capability of conventional MD simulations [35], special techniques are required to speed up the process, such as steer MD [36–38] and metadynamics [39,40]. Metadynamics works by adding an external, history-dependent bias potential that acts on a selected number of collective variables.

The folding of RNA requires cations to counter the electrostatic repulsion between backbone phosphates [41,42]. Mg^{2+}, due to its small radius and double charge, can not only directly

or indirectly interact with phosphates in the backbone but also enter the core to interact with nucleobases [41,43]. In addition to stabilizing RNA structure [44], Mg^{2+} can help mediate molecular recognition [45,46]. Because Mg^{2+} has the same number of electrons as water, locating Mg^{2+} ions in crystal structures can be a challenge [47] and requires relatively high resolution [25]. In MD simulations, ions, including Mg^{2+}, are often randomly distributed, and therefore most of them reside in the solvent [42,48]. A number of computational methods have been developed to predict Mg^{2+} sites, including MIB and IonCom based on structures or sequences for proteins (http://bioinfo.cmu.edu.tw/MIB/ [49]; https://zhanglab.ccmb.med.umich.edu/IonCom/ [50]), and MetalionRNA and MCTBI based on a knowledge-based anisotropic potential or Monte Carlo sampling for RNA (http://metalionrna.genesilico.pl/ [51]; http://rna.physics.missouri.edu/MCTBI [52,53]).

Here we report MD simulation results on the energetics and dynamics of the *Tte* $PreQ_1$ riboswitch aptamer in complex with the cognate ligands $PreQ_0$ and $PreQ_1$ and the synthetic ligands L_1, L_2, and L_3. Mg^{2+} are found to be essential in stabilizing the binding pocket for the cognate ligands. By comparing and contrasting these two groups of ligands, we learn how the chemical (e.g., number of hydrogen bond donors and acceptors) and physical (e.g., molecular size) features of ligands affect binding affinity and ligand exit paths. In particular, the reduction in the number of hydrogen bond donors and acceptors from five in the cognate group (Fig 1B) to one in the synthetic group (Fig 1C) leads to a dramatic loss in hydrogen bonding with nucleobases. The larger sizes of the synthetic group also lead to significant loosening of the binding pocket, including extrusion of the C15 nucleobase and a widening of the C15-C30 groove. Correspondingly, whereas the preferred exit of the cognate ligands is through the front door between G5 and G11, the preferred exit of the synthetic ligands is the back door between C15 and C30.

Results

We carried out a total of 153.5 μs MD simulations for the *Tte* $PreQ_1$ riboswitch aptamer bound with the cognate ligand Q_1 or Q_0, or with the synthetic ligand L_1, L_2, or L_3, or in the apo form (Table 1). Simulations were done with and without Mg^{2+} in order to uncover the effects of this important ion. In addition to conventional MD (cMD), metadynamics simulations were also run to investigate the unbinding paths of ligands. The main results are presented from the simulations with Mg^{2+}; only when comparison is made we show Mg^{2+}-free results. Most of the simulations were run using the AMBER ff99bsc0+χ_{OL3} force field [54–56] for

Table 1. Summary of molecular dynamics (MD) simulations for various systems.

System	# of Mg^{2+} ions	Type of simulations	# of replicates	Length of trajectory (μs)	Total time (μs)
Force field: ff99bsc0+χ_{OL3}/Li13					
Apo, Q_1, Q_0, L_1, L_2, L_3	7[a]	cMD	8	1	48
Apo, Q_1, Q_0, L_1, L_2, L_3	No	cMD	8	1	48
Apo	16[b]	cMD	4	1	4
Q_1, Q_0, L_1, L_2, L_3	7[a]	metadynamics	15	0.5	37.5
Force field: CUFIX/Li13					
Q_1, L_1	7[a]	cMD	4	1	8
Force field: ff99bsc0+χ_{OL3}/Allner12					
Q_1, L_1	7[a]	cMD	4	1	8

[a] Ions initially placed using MCTBI [52,53].

[b] Ions initially placed using Leap.

https://doi.org/10.1371/journal.pcbi.1009603.t001

RNA and the Li et al. [57] (Li13) parameters for Mg^{2+}. To validate the robustness of the findings, additional simulations were run using the CUFIX force field for RNA [58] along with the Li13 parameters for Mg^{2+} and the ff99bsc0+χ_{OL3} force field along with the Allner et al. [59] (Allner12) parameters for Mg^{2+}.

Free energy decomposition reveals how physicochemical features of ligands affect binding affinity

To explain the significant difference in binding affinity between the cognate and synthetic groups of ligands, we calculated the binding free energies by applying the MM-PBSA method to the second half of eight replicate cMD simulations of each RNA-ligand complex. MM-PBSA has been successfully used on many RNA-ligand [29,30] and protein-ligand [60,61] systems. Although this method can have large uncertainties in the absolute free energy calculated for a given ligand, the relative difference in binding free energy between ligands calculated from comparative MD simulations can be very informative [62]. The binding free energy consists of five terms:

$$\Delta G_{\text{bind}} = \Delta E_{\text{ele}} + \Delta E_{\text{vdW}} + \Delta G_{\text{pol}} + \Delta G_{\text{nonpol}} - T\Delta S \quad (1)$$

where ΔE_{ele} represents the average electrostatic interaction energy between the RNA and the ligand in gas phase; ΔE_{vdW} is the counterpart for van der Waals interactions; ΔG_{pol} and ΔG_{nonpol} account for the solvent environment of the RNA-ligand complex; ΔS is the change in entropy upon binding; and T is the absolute temperature. These components and the total binding free energies for the cognate and synthetic ligands, calculated from the simulations in the presence of Mg^{2+}, are listed in Table 2.

MM-PBSA predicted binding free energies of ~ -18 kcal/mol for the cognate group and close to ~1 kcal/mol for the synthetic group. Though these results exaggerate the actual difference in ΔG_{bind} (see row with heading "ΔG_{exp}" in Table 2), they do correctly predict the cognate group as the stronger binders. Comparing the two groups of ligands, the polar components ($\Delta E_{\text{ele}}+\Delta G_{\text{pol}}$) are much more favorable (by ~30 kcal/mol) to the cognate group, offset only partially (by ~10 kcal/mol) by the nonpolar components ($\Delta E_{\text{vdW}}+\Delta G_{\text{nonpol}}$) that favors the synthetic group. These contrasts can be easily attributed to the greater number of hydrogen bond donors and acceptors in the cognate group and the bulkier sizes of the synthetic group.

Table 2. Binding free energies and their components (in kcal/mol) for five ligands[a].

	Q_1	Q_0	L_1	L_2	L_3
ΔE_{ele}	-32.93±0.65	-24.26±0.90	-5.38±0.89	-4.1±0.97	-6.5±0.12
ΔE_{vdW}	-32.42±0.66	-35.56±0.08	-41.65±0.2	-45.77±1.57	-42.54±1.47
ΔG_{pol}	33.77±0.95	25.14±0.67	33.43±1.51	39.5±2.47	36.4±1.33
ΔG_{nonpol}	-3.32±0.02	-3.23±0.00	-4.31±0.03	-4.54±0.07	-4.3±0.12
$\Delta E_{\text{ele}}+\Delta G_{\text{pol}}$	0.84±1.23	0.88±0.36	28.05±0.92	35.4±2.18	29.9±1.25
$\Delta E_{\text{vdW}}+\Delta G_{\text{nonpol}}$	-35.74±0.66	-38.79±0.08	-45.96±0.18	-50.31±1.63	-46.84±1.58
ΔH	-34.9±1.46	-37.9±0.32	-17.91±0.99	-14.92±1.51	-16.94±0.75
$T\Delta S$	-16.17±0.21	-19.77±0.18	-16.97±0.27	-18.12±0.24	-18.43±0.24
ΔG_{bind}	-18.73±1.60	-18.14±0.36	-0.94±1.05	3.21±1.49	1.48±0.70
ΔG_{exp} [b]	-11.93	-10.23	-8.65	-8.54	-9.61

[a] Errors, given after the ± sign, represent standard error of the mean for a sample of eight points (each from a replicate simulation).

[b] Calculated from the experimental dissociation constants (K_D, in units of molar) [23,24] according to $\Delta G_{\text{exp}} = RT \ln K_D$, where R is the gas constant.

https://doi.org/10.1371/journal.pcbi.1009603.t002

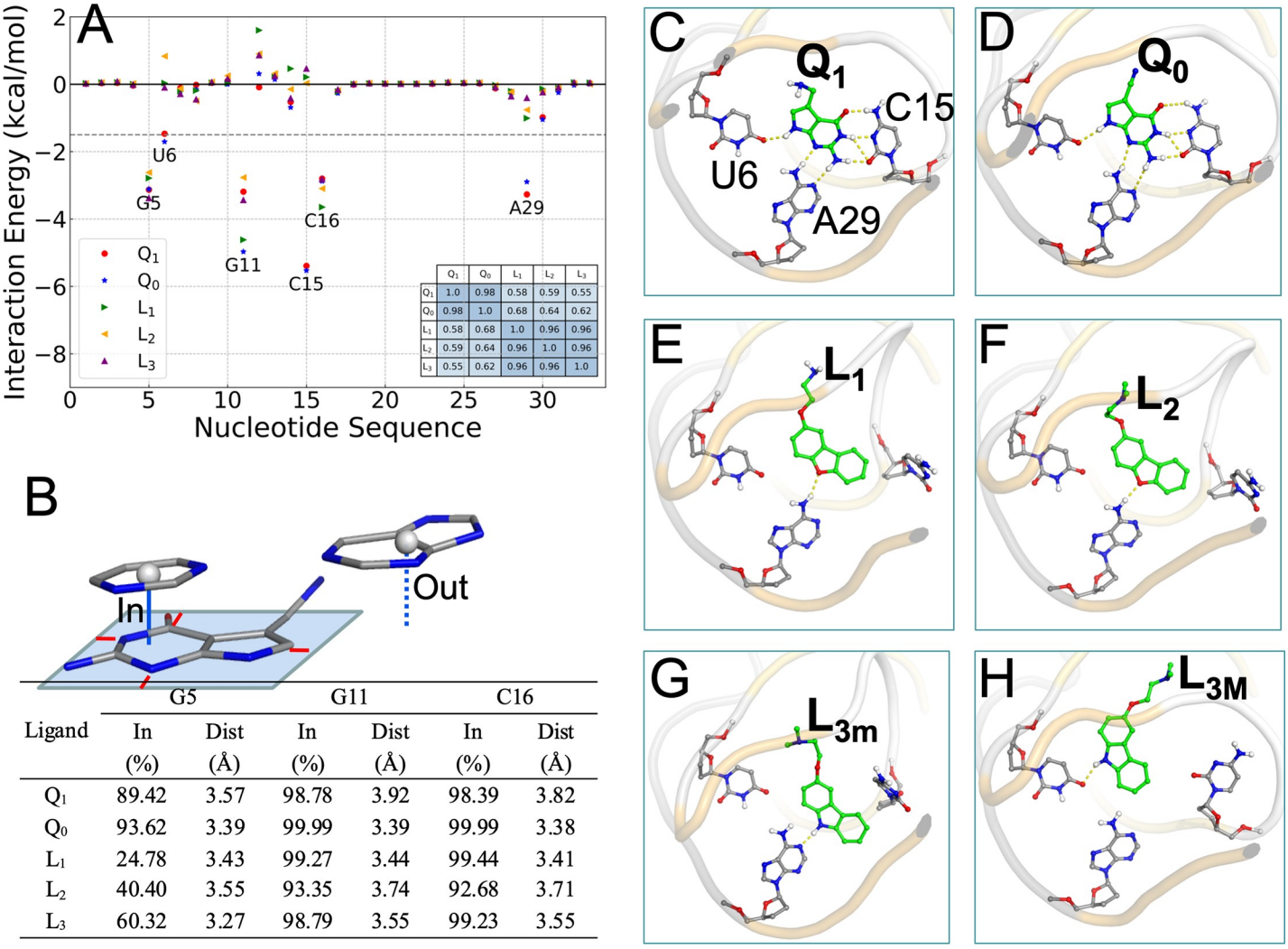

	Q_1	Q_0	L_1	L_2	L_3
Q_1	1.0	0.98	0.58	0.59	0.55
Q_0	0.98	1.0	0.68	0.64	0.62
L_1	0.58	0.68	1.0	0.96	0.96
L_2	0.59	0.64	0.96	1.0	0.96
L_3	0.55	0.62	0.96	0.96	1.0

Ligand	G5		G11		C16	
	In (%)	Dist (Å)	In (%)	Dist (Å)	In (%)	Dist (Å)
Q_1	89.42	3.57	98.78	3.92	98.39	3.82
Q_0	93.62	3.39	99.99	3.39	99.99	3.38
L_1	24.78	3.43	99.27	3.44	99.44	3.41
L_2	40.40	3.55	93.35	3.74	92.68	3.71
L_3	60.32	3.27	98.79	3.55	99.23	3.55

Fig 2. Interactions of cognate and synthetic ligands with the PreQ$_1$ aptamer in cMD simulations with Mg^{2+}. (A) Contributions of individual nucleotides to the binding free energies. A dashed horizontal line is drawn at -1.5 kcal/mol, which separates the pocket-lining nucleotides from the rest of the sequence. Inset: a table listing the correlation coefficients between the individual contributions of any two complexes. (B) Ligand-nucleotide base stacking statistics. Top: illustration of when a nucleobase is ("in") or is not ("out") in a stacking position with the ligand. A rectangle is drawn around the ligand rings atoms, with a minimum of 0.5 Å separation (shown by red lines). A cytosine is in an "in" position, with vertical distance drawn as a solid line, as the projection of its center is inside the rectangle; a guanine is in an "out" position, with vertical distance drawn as a dashed line, as the projection of its center is outside the rectangle. Bottom: in-fractions of three nucleobases and their average vertical distances from the ligand rings. (C)-(H) In-plane hydrogen bonds between ligands and nucleobases, shown as dashed lines, in representative structures from cMD simulations.

https://doi.org/10.1371/journal.pcbi.1009603.g002

To gain insight into how RNA-ligand interactions lead to the difference in affinity between the cognate and synthetic groups, we decomposed ΔG_{bind} into contributions of the 33 nucleotides of the *Tte* aptamer (Fig 2A). The correlation coefficients of these individual contributions for any two ligands are nearly 1 within both the cognate and synthetic groups, but reduces to ~0.6 between the groups (Fig 2A, inset table). This correlation analysis clearly indicates that the two groups of ligands are distinct. The only nucleotides that contribute more than 1.5 kcal/mol in at least one complex are the six that form either base stacking (G5, G11, C16) or in-plane hydrogen bonding (U6, C15, A29) with the ligands (Fig 1A). The base-stacking nucleotides contribute nearly the same to the binding free energies of the two groups of ligands, but the hydrogen-bonding nucleotides differ by 1.8, 5.7, and 2.4 kcal/mol, respectively,

in their contributions to the two groups. This result identifies in-plane hydrogen bonding as the dominant factor for the difference in affinity between the cognate and synthetic groups.

The MM-PBSA results calculated from the simulations in the absence of Mg^{2+} are presented in S1 Table and S1A Fig. The qualitative differences between the cognate and synthetic ligands described above are also valid in the Mg^{2+}-free simulations. The only major change is that the binding free energies of the cognate group become less favorable by ~10 kcal/mol, which come entirely from the polar components. The stabilization of cognate ligand binding by Mg^{2+} is explained below.

Binding poses of the five ligands differ in overt and subtle ways

Next we present structural differences around the binding pocket among the aptamer-ligand complexes in the cMD simulations. To characterize base stacking, we calculated the fraction ("in-fraction") of snapshots where a nucleobase falls within a rectangle around the ring atoms of the ligand, and among these snapshots, the vertical distance between the center of the nucleobase and the rectangle (Fig 2B, top). For the cognate ligands, the in-fractions of G5, G11, and C16 all are close to 100%, but for the synthetic ligands, the in-fractions of G5 decrease to between 25% to 60% (Fig 2B, bottom). Among the in-fractions, the distances between the nucleobases and the ligand rings are about 3.5 Å, the van der Waals contact distance for carbon atoms. A subtle but consistent difference within the cognate group is that all the three nucleobases have slightly higher in-fractions and shorter distances, thus implicating a tighter binding pocket, for Q_0 than for Q_1. The tighter binding pocket for Q_0 is consistent with the more favorable van der Waals interaction energy and the higher entropic cost listed in Table 2. In the absence of Mg^{2+}, the in-fractions of G5 decrease to below 50% for the cognate group (S1B Fig). The effect of Mg^{2+} on base stacking is more subtle for the synthetic group, with the in-fractions of G11 and C16 decreasing to between 71% to 85%.

The three nucleobases, U6, C15, A29, form six in-plane hydrogen bonds with the cognate ligands in the crystal structures (Fig 1A) [23–26]. These hydrogen bonds are well maintained in the cMD simulations with Mg^{2+} (Table 3). Fig 2C and 2D shows the typical poses of Q_1 and Q_0, respectively, in the binding pocket. In particular, the C15 nucleobase remains parallel to

Table 3. Hydrogen bonding probabilities.

Donor	Acceptor	Probability (%)	
		w/ Mg^{2+}	w/o Mg^{2+}
Q_1 / Q_0 N4	U6 O4	85.4 / 95.4[a]	92.1 / 95.6
C15 N4	Q_1 / Q_0 O1	94.9 / 92.2	42.6 / 18.9
Q_1 / Q_0 N1	C15 N3	91.3 / 95.2	43.7 / 19.4
Q_1 / Q_0 N5	C15 O2	87.7 / 96.4	52.2 / 69.0
Q_1 / Q_0 N1	C15 O2	30.7 / 45.1	71.1 / 87.8
A29 N6	Q_1 / Q_0 N2	87.8 / 98.5	98.8 / 99.7
Q_1 / Q_0 N5	A29 N1	85.5/ 82.6	95.8 / 93.8
Q_1 N3	*G5 O6 / N7*	*21.6 / 18.9*[b]	*50.3 / 6.4*
Q_1 N3	*G11 N7*	*32.6*	*20.1*
A29 N6	L_1 / L_2 O2	86.5 / 76.7	76.4 / 94.0
L_3 N1	U6 O4 / A29 N1	55.2 / 27.6	52.9/ 14.0
L_1 N1	*G5 O6 / N7*	*37.0 / 52.3*	*7.8 / 16.9*

[a] "/" separates the hydrogen bonding probabilities for two different donors or acceptors listed in the same row.

[b] Entries listed in italic are for Q_1 and L_1 methylamines as hydrogen bond donors.

https://doi.org/10.1371/journal.pcbi.1009603.t003

the ligand rings and forms three stable hydrogen bonds with Q_1 and Q_0, pairing N4, N3, and O2 of C15 with O1, N1, and N5 of Q_1 and Q_0 (S1 Movie). About one third of the time, O2 of C15 and N1 of Q_1 and Q_0 form an additional hydrogen bond. In contrast, the rings of the synthetic ligands have a single hydrogen bond donor or acceptor (compared with five for the cognate ligands) and forms a single hydrogen (Table 3). For L_1 and L_2, the O2 acceptor pairs with the A29 N6 donor, and the C15 nucleobase extrudes into an orthogonal orientation, to accommodate the synthetic ligands' bulkier size (Fig 2E and 2F). In the crystal structures of the aptamer bound with the synthetic ligands [23], L_3 is positioned similarly to L_1 and L_2 and also hydrogen bonds with A29. However, unlike L_1 and L_2, L_3 is a donor, not acceptor, and correspondingly the partner changes from N6 to N1 of A29. As a result of this change in hydrogen bonding partner, the rings of L_3 move closer to C30 (Fig 2G). In the cMD simulations, hydrogen bonding with A29 is found in only 27.6% of the snapshots (Table 3). Instead, in 55.2% of the snapshots, L_3 moves laterally to hydrogen bond with another acceptor, i.e., O4 of U6, allowing the C15 nucleobase to keep its parallel orientation (Fig 2H). We label the A29-hydrogen bonded minor and the U6-hydrogen bonded major poses as L_{3m} and L_{3M}, respectively. The L_{3m} and L_{3M} poses readily interconvert, with multiple transitions observed in each simulation (S2 Fig and S2 Movie).

Q_1 differs from Q_0 by the substitution of a methylamine for a cyano (Fig 1B). In 40.5% of the snapshots, this methylamine hydrogen bonds with O6 or N7 of G5; in another 32.6% of the snapshots the hydrogen bond partner switches to N7 of G11 (Table 3). Thus the methylamine group of Q_1, by changing the C3-C5-C6-N3 torsion angle (S1 Movie), alternates its hydrogen-bonding partner between G5 and G11. In the recent crystal structure [Protein Data Bank (PDB) entry 6VUI] [25], the methylamine group hydrogen bonds with G5, though the authors did consider but dismissed G11 as an alternative partner. L_1 also has a methylamine, and it too can hydrogen bond with O6 or N7 of G5 (Table 3). However, the methylamine in L_1 is more separated from nearest ring than in Q_1 and this greater separation prevents hydrogen bonding with G11. Indeed, when the L_1 methylamine hydrogen bonds with G5, the rings are removed from G5 and this explains why the in-fraction of G5 for L_1 is only about one half of that for L_2 (Fig 2B).

Mg^{2+} significantly affects the hydrogen bonding of the cognate ligands with C15 (Table 3; Figs 2C and 2D and S1C and S1D). Whereas C15 and Q_1 / Q_0 form three stable hydrogen bonds in the simulations with Mg^{2+}, only one stable hydrogen bond is formed in the absence Mg^{2+}, between C15 O2 and Q_1 / Q_0 N1 (or N5). This happens as the C15 nucleobase moves and tilts away from the ligand rings (see below). Since the synthetic ligands do not hydrogen bond with C15, their in-plane hydrogen bonding is not affected by Mg^{2+} (Table 3; Figs 2E–2H and S1E–S1H).

How does Mg^{2+} stabilize aptamer binding of cognate ligands?

All our MD simulations were carried out before the release of the recent crystal structures of the *Tte* aptamer in apo form and bound with Q_1 (PDB entries 6VUH and 6VUI) [25], in which three and two Mn^{2+} ions, respectively, were located in the major groove lining the ligand binding pocket. These crystal metal sites thus allowed us to test the MD simulations, with seven Mg^{2+} ions initially placed using MCTBI [52,53] (S3A Fig). In the MCTBI model, ions around an RNA molecule are divided into diffusely bound and tightly bound; the former are treated implicitly whereas the latter are treated explicitly. The free energy of diffusely bound ions is modeled by the nonlinear Poisson-Boltzmann equation, whereas the free energy of tightly bound ions is enumerated over different modes of many-ion binding, with the energy of each mode, comprising the phosphates and a set of tightly bound ions, given by the generalized Born model. As shown in Figs 3A and S3B, the crystal metal sites overlap well with the Mg^{2+} densities calculated in our

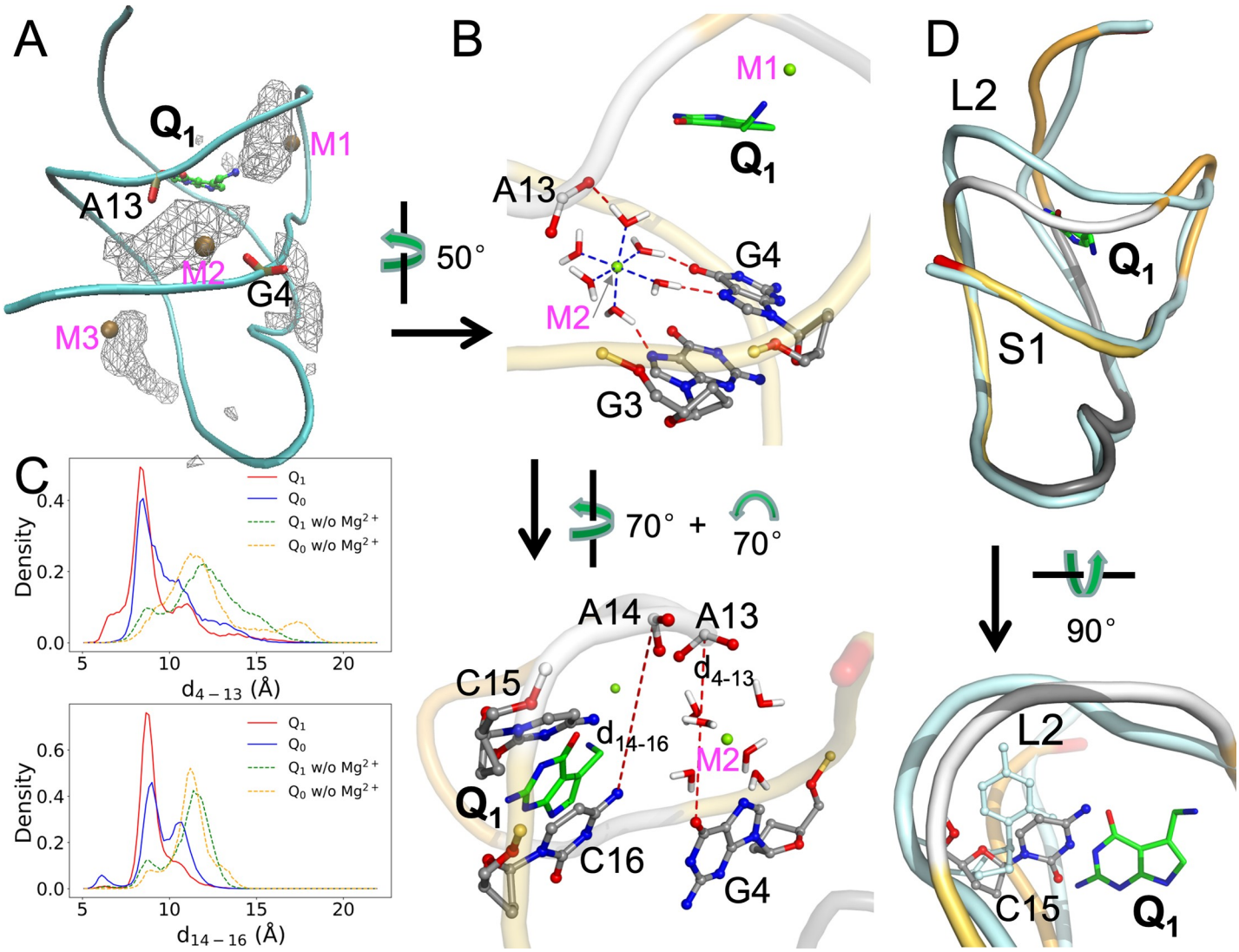

Fig 3. Distributions and effects of Mg^{2+}. (A) Density contours of Mg^{2+} ions in the Q_1-bound complex, shown as wireframe. Three Mn^{2+} ions in PDB entry 6VUI are shown as ochre spheres; the corresponding Mg^{2+} sites are labeled as M1, M2, and M3. Phosphate groups in G4 and A13 are shown in stick representation, to highlight the bridging role of M2. (B) Two views showing the coordination of the Mg^{2+} ion at the M2 site. Top: coordination of Mg^{2+} by six water molecules and the latter's hydrogen bonding with the G3 and G4 nucleobases and A14 phosphate. Bottom: two distances, $d_{4\text{-}13}$ (between G4 O6 and A13 OP1) and $d_{14\text{-}16}$ (between A14 P and C16 N4), introduced to characterize the effects of the Mg^{2+} ion. (C) Probability densities of $d_{4\text{-}13}$ and $d_{14\text{-}16}$, in cMD simulations with and without Mg^{2+} ions. (D) Effect of Mg^{2+} ions on the separation of the L2 loop from the S1 helix in the Q_1-bound form. Two representative structures are superimposed, with the aptamer in the presence of Mg^{2+} shown in the same multi-color scheme as in Fig 1A and the aptamer in the absence of Mg^{2+} shown in a uniform cyan color. In the bottom view, the C15 nucleotides in the two structures are shown in a stick representation.

https://doi.org/10.1371/journal.pcbi.1009603.g003

cMD simulations of the Q_1-bound and apo forms. The Mg^{2+} densities in the Q_0-bound form also overlap well with the Q_1 crystal metal sites (S3C Fig), whereas the densities in the complexes with the synthetic ligands overlap well with the apo crystal metal sites (S3D Fig). We label these sites as M1, M2 (M2'), M3, and M4. We also tested initial Mg^{2+} ion placement in the apo form using the Leap module in AMBER18 [63], which finds ion binding sites on a grid according to the Coulomb potential of the RNA. The Mg^{2+} densities in these simulations are similar to those started with MCTBI placement (S4 Fig), demonstrating that the Mg^{2+} ion sites found in the cMD simulations are robust and insensitive to the precise initial placement. Each Mg^{2+} ion coordinates with six polar groups (Fig 3B, top panel).

Of particular importance is a deep site, M2, in the complexes with the cognate ligands, where Mg^{2+} bridges between G4 and G3 on the S1 helix and A13 on the L2 loop (Fig 3B). To present a full picture of this bridging effect in the MD simulations, we monitored two distances between S1 and L2: $d_{4\text{-}13}$ between A4 O6 and A13 OP1; and $d_{14\text{-}16}$ between A14 P and C16 N4 (Fig 3B, bottom panel). The probability densities of these two distances both peak around 8.5 Å (Fig 3C). In the simulations without Mg^{2+}, the peaks shift to larger distances by 2 to 4 Å, indicating a greater separation of L2 from S1. The increased separation is also evident when representative structures from the simulations of the Q_1-bound aptamer with and without Mg^{2+} are superimposed (Fig 3D, top panel). The further separation of L2 from S1 creates new room for C15 (Fig 3D, bottom panel), which as noted above moves and tilts away from the cognate ligand rings in the absence of Mg^{2+} (compare Figs 2C and S1C). Very similar differences are also observed in the simulations of the Q_0-bound aptamer with and without Mg^{2+} (Figs 3C and S3E; also compare Figs 2D and S1D). Therefore Mg^{2+} is essential in maintaining C15 in a position to form stable hydrogen bonds with the cognate ligands.

Simulations with alternative force fields confirm the differential stabilization of aptamer complexes with cognate and synthetic ligands

The simulations reported above were run using ff99bsc0+χ_{OL3} for RNA and Li13 for Mg^{2+}. To check the robustness of the resulting findings regarding the energetic and structural differences between the aptamer complexes bound with cognate and synthetic ligands, we ran additional simulations using alternative force fields for RNA and Mg^{2+}. The alternative RNA force field was CUFIX [58], which was based on ff99bsc0 but with modifications for Lennard-Jones parameters of selected atom types, including phosphate oxygen atoms. The alternative parameter set for Mg^{2+} was Allner12 [59], which was optimized to fit experimental data for residence times of coordinated water molecules. For both the Q_1- and L_1-bound aptamers, we ran simulations using CUFIX paired with Li13 and using ff99bsc0+χ_{OL3} paired with Allner12.

In S2 Table, we compare the binding free energies of Q_1 and L_1 from the ff99bsc0+χ_{OL3}/Li13 original simulations with those from the CUFIX/Li13 and ff99bsc0+χ_{OL3}/Allner12 simulations. The large difference in binding free energy between Q_1 and L_1 from the original simulations are reproduced by the additional simulations. Moreover, upon decomposition, the contributions of individual nucleotides correlate extremely well among the three force field combinations, with correlation coefficients at 0.98 to 1.00.

The probabilities of Q_1 and L_1 hydrogen bonding with nucleotides in the original simulations are also well reproduced in the additional simulations (S3 Table). The probabilities of two hydrogen bonds, between the O1 atom of Q_1 and the N4 atom of nucleotide C15 and between the N1 atom of Q_1 and the N3 atom of this nucleotide, have modest reductions (from ~90% to ~70%) in the additional simulations, compensated by slightly higher probabilities of three other hydrogen bonds. Lastly, the Mg^{2+} densities in the additional simulations of the Q_1- and L_1-bound aptamers are very similar to those in the original simulations (S5 Fig). Again, Mg^{2+} densities in the Q_1-bound form have a single peak around the M2 site as found in the Q_1-bound crystal structure (PDB entry 6VUI), but two peaks, around M2 and M2', as found in the apo crystal (PDB entry 6VUH). Below we return to results obtained by simulations using ff99bsc0+χ_{OL3}/Li13.

The Aptamer bound with synthetic ligands resembles the apo state

Connolly et al. [23] recognized two key differences between the Q_1- and L_1-bound structures and concluded that the latter structure is similar to the apo state. The first, already described above, is the extrusion of the C15 nucleobase into an orthogonal orientation (Fig 2C and 2E).

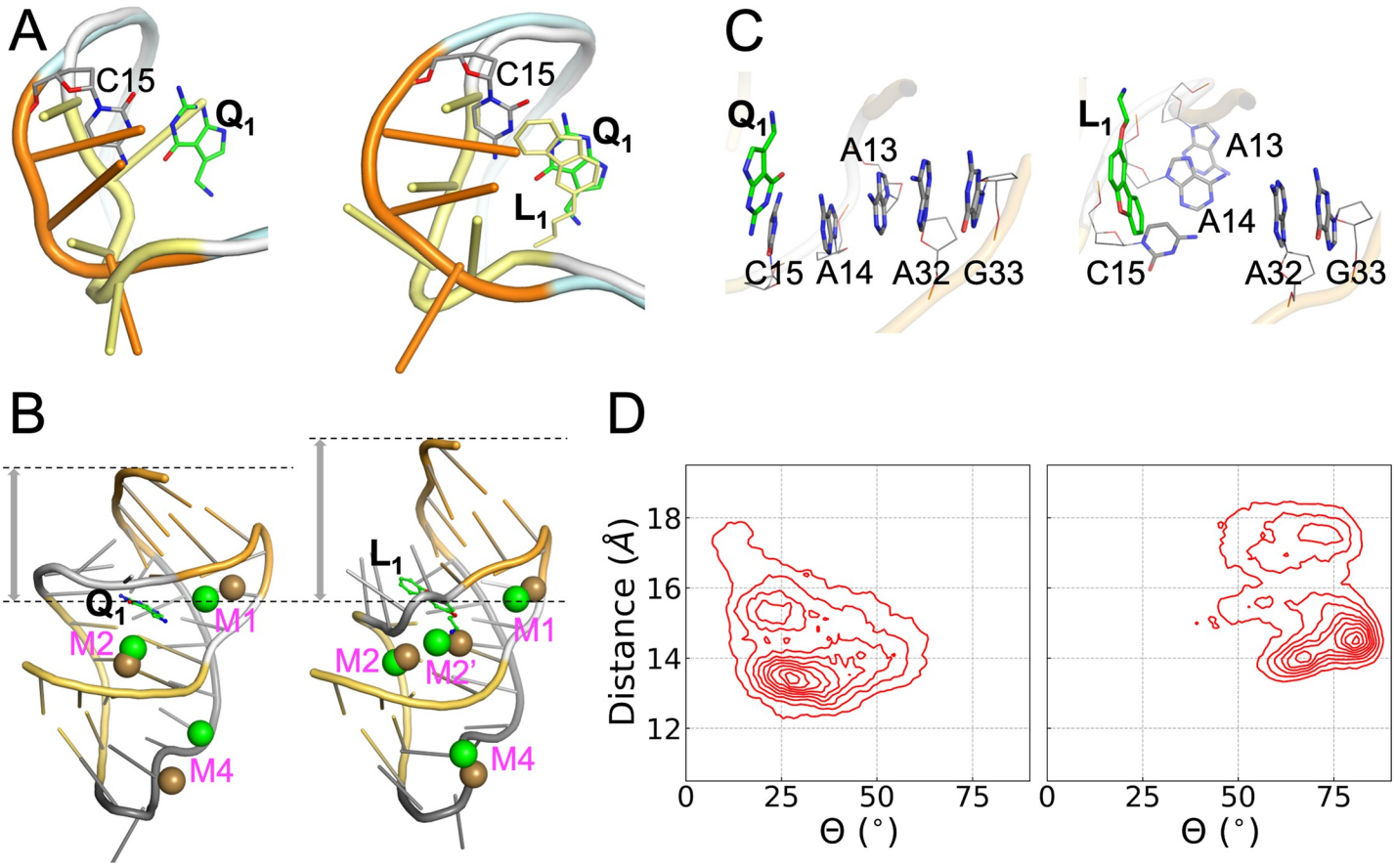

Fig 4. Contrast between Q_1- and L_1-bound complexes. (A) Conformations of the L2 loop (U12-A13-A14-C15). Left: conformations adopted in the apo (yellow) and Q_1-bound (orange) forms, from PDB entries 6VUH and 3Q50, respectively. Right: conformations in representative structures of the L_1-bound (yellow) and Q_1-bound (orange) forms from cMD simulations. (B) Comparison between representative Mg^{2+} sites from cMD simulations and Mn^{2+} positions from crystal structures (PDB entries 6VUI and 6VUH). Left: similarity between cMD Mg^{2+} (green) and crystal Mn^{2+} (ochre) positions in the Q_1-bound form. Right: similarity between cMD Mg^{2+} (green) positions in the L_1-bound from and crystal Mn^{2+} (ochre) positions in the apo form. The L_1-bound structure has a larger separation between the ligand and the 3' end. (C) The orthogonal orientations of the C15-A14-A13 nucleobases in the Q_1- and L_1-bound forms in cMD simulations, leading to one stack or two separate stacks, respectively, with the A32-G33 nucleobases. (D) Density maps in the space of two collective variables: the distance from the center of the binding pocket to the center of the A32 and G33 nucleobases, and the average angle (Θ) between the A13, A14, and C15 nucleobases and the A32 and G33 nucleobases.

https://doi.org/10.1371/journal.pcbi.1009603.g004

The second is a farther separation of the A32 and G33 nucleobases from the ligand rings in the L_1-bound structure. However, the latter crystal structure was determined with the A13 and A14 nucleobases removed, and thus represented an incomplete picture. Our MD simulations of the complete aptamer now provide strong additional support for the conclusion that the structures bound with the synthetic ligands are similar to the apo state.

First, the L2 loop adopts distinct conformations in the apo and Q_1-bound structures (PDB entries 6VUH and 3Q50 [24,25]; Fig 4A, left panel). In the apo structure, L2 is closer toward the ligand binding pocket to allow the insertion of the A14 nucleobase into the pocket. L2 in our simulations of the L_1-bound aptamer adopts a similar "close" conformation, although the A14 nucleobase is extruded to accommodate the presence of the ligand (Fig 4A, right panel). Second, as noted above, Mg^{2+} densities in our simulations of the Q_1-bound aptamer overlap with Mn^{2+} ions found in the Q_1-bound structure (PDB entry 6VUI) [25] (Figs 3A; 4B, left panel; and S5, top row). In contrast, Mg^{2+} densities in the L_1-bound aptamer overlap with Mn^{2+} ions found in the apo structure (PDB entry 6VUH) [25] (Figs S3D; 4B, right panel; and S5, bottom row). Finally and most importantly, in our simulations of the Q_1-bound aptamer,

three nucleotides from the L2 loop, C15, A14, and A13, maintain continuous base stack with two nucleotides, A32 and G33 (the Shine-Dalgarno sequence), in the S2 helix (Fig 4C, left panel). The continuous base stack is crucial for inhibiting gene expression by sequestrating the Shine-Dalgarno sequence from recognition by the ribosome [25]. However, in the simulations of the L_1-bound aptamer, the L2 nucleotides and the S2 nucleotides form two separate stacks (Fig 4C, right panel). Both A14 and A13 take the orthogonal orientation of C15 to form a base stack that is disengaged from the A32-G33 stack. In the apo crystal structure, both C15 and A13 have the orthogonal orientation (Fig 4A, left panel).

To gain a global sense on the difference in conformational space sampled by the Q_1- and L_1-bound aptamers, in Fig 4D we present their density maps over two functionally important collective variables. One of these variables is the distance of the A32 and G33 nucleobases from the binding pocket (Fig 4B); the other is the average angle between the A32 and G33 nucleobases and the A13, A14, and C15 nucleobases (Fig 4C). For the Q_1-bound aptamer, the highest density occurs at a distance of 13.5 Å and an angle of 27.5˚. For the L_1-bound aptamer, the peak density moves to a larger distance of 14.5 Å and a much larger angle of 80.5˚. These differences are already illustrated in Fig 4B and 4C. However, the density maps cover relatively broad regions, with other local minima.

The synthetic ligands lead to loosening at the back of the binding pocket

We now examine the total volume explored by the atoms of each ligand in the cMD simulations, by calculating the density contour of the ligand (Fig 5A–5C). In line with the foregoing observation that the binding pocket is tight for Q_0 (Fig 2B, bottom), this cognate ligand shows a very compact density contour (Fig 5A, green). The density contour of Q_1 (Fig 5A, red) is slightly expanded around the rings, and there is also extra density for the methylamine "head" group.

The density contours of L_1 and L_2 are further expanded, at both the back (facing the C15-C30 groove) and the front (facing the G5-G11 groove) (Fig 5B). At the back, the expansion, due to the additional ring, would clash with the C15 nucleobase and leads to its extrusion into an orthogonal orientation. At the front, the expansion is largely due to the longer head group (compare Fig 1B and 1C). This front expansion, both longitudinally and laterally, is especially prominent for L_2, which has two extra terminal methyls in the head group. The aforementioned possibility of the L_1 methylamine hydrogen bonding with G5 leads to a retraction of the rings toward the back, accounting for the greater back expansion of L_1 relative to L_2. As described above, L_3 readily switches between two poses, L_{3m} (hydrogen bonding with A29) and L_{3M} (hydrogen bonding with U6) (S2 Fig and S2 Movie). The density contour of L_{3m} (Fig 5C, red) moves slightly farther toward the back than that of L_1, due to the change in hydrogen bonding partner from N6 to N1 of A29 (Fig 2E and 2G). Meanwhile, the density contour of L_{3M} (Fig 5C, green) moves toward the front, passing that of L_2.

The deeper penetration into the back of the binding pocket by L_1, L_2, and L_{3m} relative to the cognate ligands are illustrated by snapshots shown in Figs 5D–5F and S6A. In one of the eight simulations of the L_3-bound aptamer (S2 Fig, MD4), a major portion of the ligand rings is even transiently positioned outside the back door between C15 and C30 (Fig 5F). In two simulations without Mg^{2+}, L_3 escaped altogether through the back door.

To gauge the width of the back door, we monitored the distance ($d_{15\text{-}30}$) between the C1' atoms of C15 and C30 (Figs 5D–5F and S6A). The $d_{15\text{-}30}$ probability densities in the simulations of the apo and five bound forms are shown in Fig 5G. The mean ± standard deviation of $d_{15\text{-}30}$ in the apo form is 7.8 ± 1.6 Å. The mean value is preserved by the cognate ligands (7.3 ± 0.6 Å for Q_1; 7.7 ± 0.8 Å for Q_0), but is significantly elevated by the synthetic ligands

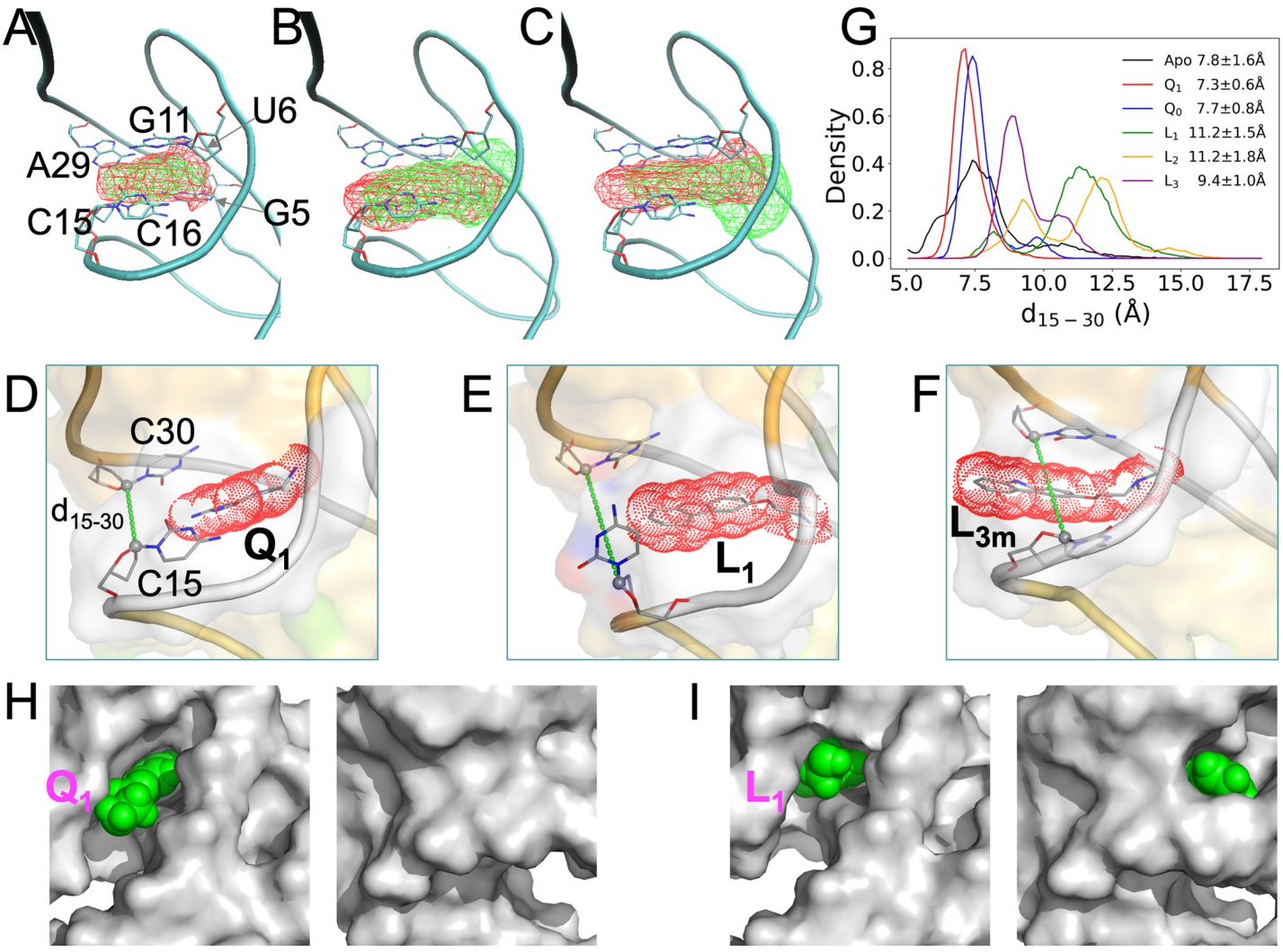

Fig 5. Loosening in the back of the binding pocket when bound with synthetic ligands, in cMD simulations with Mg^{2+}. (A)-(C) Density contours of ligands, shown as wireframe in reference to a representative Q_1-bound structure, with the six pocket-lining nucleotides displayed in stick representation. Panel (A) shows contours in red for Q_1 and in green for Q_0; panel (B) shows contours in red for L_1 and in green for L_2; and panel (C) shows contours in red for L_{3m} and in green for L_{3M}. The L_{3m} and L_{3M} contours were calculated only from snapshots where hydrogen bonding with A29 or U6 was present. (D)-(F) Representative conformations of the Q_1-, L_1-, and L_{3m}-bound forms, respectively. Ligands are shown in both stick representation and as dot surface. The C1' atoms of C15 and C30 are connected to define the distance $d_{15\text{-}30}$ and to illustrate the back door. (G) The probability densities of $d_{15\text{-}30}$ in the apo form and the five liganded forms. (H) Two views into Q_1 in the binding pocket. The aptamer is shown as gray surface while the ligand is shown as green spheres. Left: front view showing Q_1 exposure; right: back view showing buried Q_1. (I) Corresponding presentation for L_1, except that this ligand is exposed both on the front and on the back.

https://doi.org/10.1371/journal.pcbi.1009603.g005

(11.2 ± 1.5 Å for L_1; 11.2 ± 1.8 Å for L_2; 9.4 ± 1.0 Å for L_3). Similar results are also obtained from the cMD simulations without Mg^{2+} (S6B Fig).

Another distance, $d_{5\text{-}11}$, between the Cl' atoms of G5 and G11 was also monitored to gauge the width of the front door (S6C and S6D Fig). The five bound forms do not show significant differences in $d_{5\text{-}11}$ among themselves, but their mean $d_{5\text{-}11}$ values, around 12 Å, are larger by 1 to 2 Å than the apo counterpart. Similar mean $d_{5\text{-}11}$ values are found for the five bound forms with and without Mg^{2+}, but for the apo form, $d_{5\text{-}11}$ shifts to larger values (by ~2 Å) when Mg^{2+} is absent (S6E Fig).

In short, our cMD simulations reveal that, whereas the cognate ligands maintain the intrinsic width of the back door (as found in the apo form), the synthetic ligands widen this door

and, in the case of L_3, can even partially slip through it. In contrast, the front door is kept to approximately the same width by the cognate and synthetic ligands. Consequently, while both the cognate and synthetic ligands are mostly buried in the binding pocket, the cognate ligands are exposed at the front (Figs 5H and S6F) but the synthetic ligands are exposed at both the front and the back (Figs 5I and S6G–S6H).

Cognate and synthetic ligands unbind through opposite pathways

The fact that Q_1 and Q_0 are exposed only at the front suggests that the cognate ligands bind and unbind through the front door. On the other hand, the exposure of the synthetic ligands at both the front and the back and the (partial) escape of L_3 through the back door suggest that these ligands may enter and exit through both doors. To investigate the unbinding and rebinding pathways, we carried out 15 well-tempered metadynamics [40] simulations for each ligand. In these simulations, biases were introduced to flatten the potential of mean force along a collective variable, here defined as the distance, r, from the center of the ligand to the center of the binding pocket (lined by the six nucleotides G5, U6, G11, C15, C16, and C30). The biases were gradually reduced during the 500 ns simulations. The trajectories of the ligands are illustrated in Figs 6A and S7A.

To determine whether unbinding or rebinding occurred through the front door (between G5 and G11) or back door (between C15 and C30) (Fig 6B), we introduced a plane passing through the C1' atoms of U6 and A10 and the C4 atom of C15, which bisects the binding pocket (Figs 6A and S7A). We defined its normal vector, pointing from the back to the front of the binding pocket, as the z axis. Along each ligand trajectory, we monitored both r and its z component (Figs 6C and S7B). The first increase of r to 9 Å was labeled as an unbinding event, whereas the next decrease of r to 1 Å was labeled as a rebinding event; and this label was repeated till the end of the trajectory. Depending on whether z was positive or negative when the unbinding or rebinding event occurred, the passage was through the front door or back door. Due to the large biases at the beginning of each simulation, the ligand very rapidly left the binding pocket. We started counting only from the subsequent rebinding event.

The total numbers of unbinding and rebinding events for each ligand are listed in Table 4. For the cognate ligands, unbinding shows a significant preference for the front door. Q_1 has 14 events through the front door but only 4 events through the back door (S3 Movie); for Q_0, the counts are 11 versus 6. In contrast, the overwhelming preference for synthetic ligand unbinding is through the back door, with a total of 63 events (S4 Movie). The total number of front-door unbinding events is only 9 for these ligands.

The opposite preferences of the cognate and synthetic ligands also carry over to rebinding, though the preferences are somewhat blunted for both types of ligands. For cognate ligand rebinding, there is only a modest preference for the front door (11 events each for Q_1 and Q_0, compared with 9 and 7 events, respectively, for the back). For the synthetic ligand rebinding, the total number of events through the back door is 61, while the counterpart through the front door is 17. The preference for the back door is still significant but not as overwhelming as found for unbinding.

Discussion

We have investigated the molecular determinants underlying the binding of the $PreQ_1$ riboswitch aptamer to cognate and synthetic ligands by combining conventional MD simulations, free energy decomposition, and metadynamics simulations. The analyses on structural, energetic, and dynamic properties have advanced our understanding on both the overt differences between the cognate and synthetic groups of ligands and subtle differences within each group

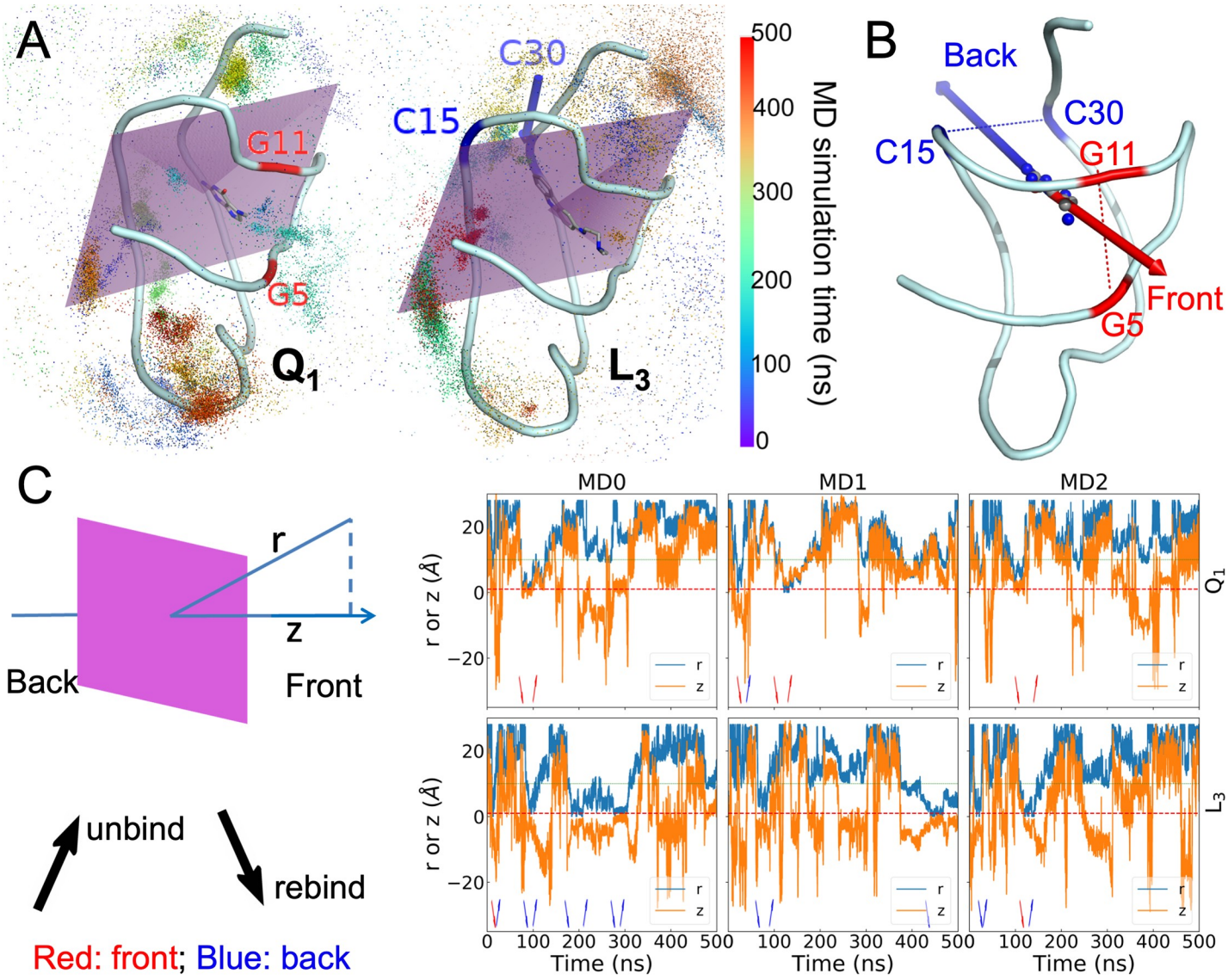

Fig 6. Unbinding and rebinding pathways of ligands. (A) The trajectories of ligand centers shown as dots colored according to the MD simulation time. The aptamer and bound ligands are shown in cartoon and stick representations, respectively. Left: Q_1; right: L_3. A plane in purple bisects the binding pocket into the front half and the back half. Two nucleotides defining the front door in the Q_1-bound complex are labeled in red; two nucleotides defining the back door in the L_3-bound complex are labeled in blue. (B) The front and back unbinding paths. (C) The center-to-center distance r between the ligand and the binding pocket and the z coordinate of the ligand center along the normal of the pocket-bisecting plane. The left-most panel illustrates r and z, and presents interpretations of arrow directions and colors that appear in the right three panels, which show time traces of r and z in three metadynamics simulations. Red dashed and green dotted horizontal lines are drawn at r = 1 and 9 Å, respectively, to indicate the times of entrance to and exit from the binding pocket.

https://doi.org/10.1371/journal.pcbi.1009603.g006

Table 4. Unbinding and rebinding events.

Ligand	Unbinding		Rebinding	
	Front	Back	Front	Back
Q_1	14	4	11	9
Q_0	11	6	11	7
L_1	5	17	7	16
L_2	2	25	7	22
L_3	2	21	3	23

https://doi.org/10.1371/journal.pcbi.1009603.t004

of ligands. In particular, the reduction of hydrogen bond donors and acceptors is the main reason for the decreased binding affinities of the synthetic ligands, while the increase in rings resulting in the opening of a back door to the binding pocket.

Our work has demonstrated the power of molecular dynamics simulations in complementing structure determination and binding assays to provide crucial missing links. For example, the L2 loop is essential both for stabilizing ligands and for communicating ligand binding to the Shine-Dalgarno sequence for downstream signaling. Yet this loop is highly dynamic and nucleobases in the loop were cleaved [23] or subject to distortion by crystal contacts [25] in structure determination. Our MD simulations have now shown how this loop responds to the synthetic ligands (by extruding to form a base stack orthogonal to that formed when bound with the cognate ligands; Fig 4C) or to Mg^{2+} (which ties L2 to S1 to keep C15 in a position to form stable hydrogen bonds with the cognate ligands; Fig 3D). Moreover, our MD simulations have found that the methylamine head group of Q_1 samples different torsion angles to alternate its hydrogen-bonding partner between G5 and G11, and L_3 samples different poses to alternate its hydrogen-bonding partner between U6 and A29. Most interestingly, our MD simulations have revealed that ligands can enter and exit the binding pocket through multiple pathways and the cognate and synthetic ligands have opposite preferences. We hope that both our specific lessons on the $PreQ_1$ riboswitch and our approach will provide guidance for designing riboswitch ligands in the future.

Our MD simulations, totaling 153.5 μs, can be considered extensive. Some of the simulations were added specifically to validate the robustness of the findings. For example, we compared two methods for initial placement of Mg^{2+} ions, and found very similar Mg^{2+} densities in the subsequent simulations. In addition, we compared energetic and structural properties calculated from three different force field combinations for RNA and Mg^{2+}, and found the results to agree well with each other. Our simulations are also directly validated by experimental data–the Mg^{2+} densities in the simulations, started from earlier crystal structures without metal ions, match well with those found in recent crystal structures.

A number of experiments can be designed to further test the predictions of our MD simulations. First, we have found that the number of hydrogen bond donors and acceptors is a key determinant for RNA binding affinity, and in large part explains the weaker affinities of the synthetic ligands. This conclusion can be tested by synthesizing analogs of L_1, L_2, and L_3 with C-C or C-H bonds replaced by polar covalent bonds. Second, we have predicted that the Q_1 methylamine can form alternative hydrogen bonds, with either the G5 nucleobase or the G11 nucleobase. Moreover, the entire L_3 ligand can have alternative poses, with hydrogen bonding to either the U6 nucleobase or the A29 nucleobase. These predictions can be tested by NMR experiments. Lastly, the opposite unbinding pathways of the cognate and synthetic ligands revealed by our simulations can also be tested experimentally. One potential method is to use small molecules called minor groove binders, to selectively block the front exit or the back exit. If our simulation results are correct, a minor groove binder that blocks the front exit will significantly impede the unbinding of the cognate ligands but have little effect on the unbinding of the synthetic ligands, while the opposite is expected for a minor groove binder that blocks the back exit. A second potential method is to introduce nucleobase analog FRET-pairs [64], which might be able to capture transient opening of the front or back exit.

Methods

Preparation of molecular systems

Initial structures of the $PreQ_1$ riboswitch aptamer bound with Q_1, L_1, L_2, and L_3 were taken from PDB entries 6E1W, 6E1S, 6E1U, and 6E1V, respectively [23]. The missing nucleotides

were transplanted from an earlier Q_1-bound structure in PDB entry 3Q50 [24]. The Q_0-bound complex was generated from the Q_1-bound complex by substituting the ligands. The apo form was generated by stripping Q_1 from the Q_1-bound complex. Missing hydrogen atoms of the aptamer were added by using the Leap module in AMBER18 [63]. The structures of the ligands were optimized using the Gaussian 16 program [65] at the HF/6–31G* level. Note that our MD simulations were completed before the release of PDB entries 6VUH and 6VUI containing the apo and Q_1-bound structures, respectively, in which Mn^{2+} ions were resolved.

Each structure was then solvated in a truncated octahedron periodic box of TIP3P [66] water molecules with a 12 Å buffer. Systems were prepared both without and with Mg^{2+}. The primary method for adding Mg^{2+} was MCTBI [52,53], which identified seven sites. Alternatively, we placed 16 Mg^{2+} ions in the solvent by using the Leap module. Additional Na^+ ions were added to neutralize the charges of systems with and without Mg^{2+} ions.

Force-field parameters of the ligands were from the restrained electrostatic potential charges and the general Amber force field [67]. The parameters for Na^+ ions were from Joung and Cheatham [68]. In most of the simulations, the force field for RNA, denoted as ff99bsc0+χ_{OL3}, was an improved version of AMBER ff99 [54], with correction for α/γ dihedrals (bsc0) [55] and correction for χ dihedrals (χ_{OL3}) [56]. The parameters for Mg^{2+} ions were from Li et al. [57] (Li13). Some simulations were also repeated using two other force field combinations for RNA and Mg^{2+}. One paired the CUFIX force field for RNA [58] with Li13 for Mg^{2+}; the other paired the ff99bsc0+χ_{OL3} force field for RNA with Mg^{2+} parameters from Aller et al. [59] (Allner12).

Conventional MD simulations

All cMD simulations were carried out by running the AMBER18 package [63]. Each system was minimized by 2500 steps of steepest descent and 2500 steps of conjugate gradient. The system was then heated from 100 K to 300 K over 50 ps and maintained at 300 K for 50 ps under constant volume. Subsequently the simulation was at constant temperature and pressure for 50 ps to adjust the solvent density. Up to this point, harmonic restraints at a force constant of 5 kcal/mol·$Å^2$ were imposed on all solute atoms except those on the L2 loop and nucleotides 16 and 33. The last step of equilibration was simulation at constant temperature and pressure for 1 ns, without any restraint. The temperature (300 K) was regulated by the Langevin thermostat [69] and pressure (1 atm) was regulated by the Berendsen barostat [70]. Covalent bonds involving hydrogen atoms were treated with the SHAKE algorithm [71] to allow for a time step of 2 fs. The particle mesh Ewald method [72] was applied to treat long-range electrostatic interactions, with the nonbonded cutoff at 12 Å. Eight replicate simulations of all the systems were carried out using ff99bsc0+χ_{OL3}/Li13 for 1 μs at constant temperature and pressure. Additionally, four replicate simulations of the Q_1- and L_1-bound forms were carried out using both the CUFIX/Li13 and the ff99bsc0+χ_{OL3}/Allner12 force fields. Snapshots were saved every 10 ps for later analysis.

Binding free energy calculations

Binding free energies and the decomposition into contributions of individual nucleotides were obtained by the MM-PBSA method [34]. For each snapshot of the simulations, the binding free energy was calculated according to Eq (1), where "Δ" means the difference between the complex and the separated RNA and ligand. ΔE_{ele} was from the Coulomb interactions between the RNA and ligand partial charges, and ΔE_{vdW} was from the van der Waals interactions between RNA and ligand atoms. Both ΔE_{ele} and ΔE_{vdW} were calculated without applying a cutoff. ΔG_{pol} was calculated by a finite-difference solution of the Poisson-Boltzmann equation at 0

salt concentration. A cubic grid with 0.4 Å spacing was employed, and 5000 linear iterations were performed. The solute and solvent dielectric constants were 1 and 80, respectively. The dielectric boundary between solute and solvent was the molecular surface defined by a 1.4 Å probe radii. $\Delta G_{\mathrm{nonpol}}$ was estimated from the solvent-accessible surface area (SASA, also using a 1.4 Å probe radii) as γSASA+β [73], where the surface tension constant γ and the correction constant β were 0.00542 kcal/mol·Å^2 and 0.92 kcal/mol, respectively. The atomic radii for both ΔG_{pol} and $\Delta G_{\mathrm{nonpol}}$ calculations were taken from the PARSE parameter set [74].

Entropies were obtained using the *nmode* module of AMBER18 [63]. Prior to the normal mode calculation, each snapshot was energy-minimized using conjugated gradient in vacuum without cutoff for nonbonded interactions. A distance-dependent dielectric constant of 4*r* was used to mimic solvent screening. The minimization was stopped either when the root-mean-square of the elements of the gradient vector reached 10^{-4} kcal/mol·Å or the number of cycles reached 50000. After performing normal mode analysis, the vibrational entropy was obtained by adding up the contributions from all the nonzero-frequency normal modes, each treated as a quantum harmonic oscillator. The translational and rotational entropies were then added to yield the total entropy. This entropy calculation was done once for the RNA-ligand complex, once for the RNA (with the ligand stripped), and once for the ligand (with the RNA stripped). Finally ΔS was obtained as the difference in entropy between the complex and the separated RNA and ligand.

From each replicate simulation, 2500 snapshots were extracted from the second 500 ns, resulting in a total of, e.g., 20,000 snapshots among 8 replicates, for the MM-PBSA calculations on each ligand. Decomposition into contributions of individual nucleotides was done only for the enthalpic components (ΔE_{ele}, ΔE_{vdW}, ΔG_{pol} and $\Delta G_{\mathrm{nonpol}}$).

Other analyses

Vertical distance in Figs 2B and z in 6B were calculated using tcl scripts in VMD [75]. All other distances and hydrogen bond formation were determined by the CPPTRAJ program [76]. Hydrogen bond criteria were donor-acceptor distance < 3.5 Å and donor-H-acceptor angle $> 120^{\circ}$. Densities of ligands and of Mg^{2+} were calculated from saved snapshots of the cMD simulations by using the *water-hist* program in the LOOS package [77].

Well-tempered metadynamics simulations

Well-tempered metadynamics simulations were as described [40]. In this method, Gaussian functions were applied to fill up wells in the potential of mean force for a collective variable. We chose the distance r from the center of the ligand to the center of the binding pocket (defined by the six nucleotide G5, U6, G11, C15, C16, and C30) as the collective variable. The Gaussian widths was set to 0.5 Å, and the Gaussian hills height was initially set at 1.2 kcal/mol and was gradually decreased with a bias factor of 15 over the course of the simulation. A soft harmonic restraining potential was also applied on the center of the ligand to keep the ligand close to the RNA. Fifteen metadynamics simulations using ff99bsc0+χ_{OL3}/Li13 were run for 500 ns each, utilizing the PLUMED v2.3 [78] plugin to the GROMACS 5.1.2 package [79].

Supporting information

S1 Table. Binding free energies and their components (in kcal/mol) for five ligands in the absence Mg2+[a].
(DOCX)

S2 Table. Binding free energies (ΔG_{bind}, in kcal/mol) for two ligands, calculated from simulations using three different force fields.
(DOCX)

S3 Table. Hydrogen bonding probabilities of two ligands, calculated from simulations using three different force fields.
(DOCX)

S1 Fig. Interactions of cognate and synthetic ligands with the $PreQ_1$ aptamer in cMD simulations without Mg^{2+}. (A) Contributions of individual nucleotides to the binding free energies. A dashed horizontal line is drawn at -1.5 kcal/mol, which separates the pocket-lining nucleotides from the rest of the sequence. Inset: a table listing the correlation coefficients between the individual contributions of any two complexes. (B) In-fractions of three nucleobases and their average vertical distances from the ligand rings. (C)-(H) In-plane hydrogen bonds between ligands and nucleobases, shown as dashed lines, in representative conformations from cMD simulations.
(TIF)

S2 Fig. Rapid switch of L_3 between two poses: one hydrogen-bonded with U6 and the other hydrogen-bonded with A29. The distances of the L_3 N1 atom from the U6 O4 and A29 N1 atoms are shown as red and blue traces along the simulation time, in eight cMD simulations. In each panel, a horizontal dashed line is drawn at 3.5 Å. The horizontal bar at the bottom is colored red or blue, according to whether the U6 or the A29 distance is $<$ 3.5 Å. The blue sections are raised slightly to better distinguish from the red sections. The bottom right panel shows an enlarged view of the blue and red sections of the horizontal bar. The MD4 simulation is special as the ligand partially slipped through the back door around 500 ns, pushing A29 out of the binding pocket; the ligand rings then flipped and retracked, leading to large distances from A29. Accordingly the upper bound of the ordinate is increased from 11 Å to 20 Å.
(TIF)

S3 Fig. Distributions and effects of Mg^{2+}. (A) Seven Mg^{2+} ions added by the MCTBI method, initially at shallow positions along two grooves of the aptamer. (B) Density contours of Mg^{2+} ions in the apo form, shown as wireframe. Five Mn^{2+} ions in PDB entry 6VUH are shown as ochre spheres; the corresponding Mg^{2+} sites are labeled as M1, M2, M2', M3, and M4. Phosphate groups in G4 and A13 are shown in stick representation. (C) Corresponding presentation for the Q_0-bound form, except that four crystal Mn^{2+} ions from PDB entry 6VUI are shown, with the sites labeled as M1, M2, M3, and M4. (D) Presentations for the L_1-, L_2-, and L_{3m}-bound forms, very similar to that shown in panel (B) for the apo form. (E) Effect of Mg^{2+} ions on the separation of the L2 loop from the S1 helix in the Q_0-bound form. Two representative structures are superimposed, with the aptamer in the presence of Mg^{2+} shown in the same multi-color scheme as in Fig 1A and the aptamer in the absence of Mg^{2+} shown in a uniform cyan color. In the bottom view, the C15 nucleotides in the two structures are shown in a stick representation.
(TIF)

S4 Fig. Distributions Mg^{2+} ions in simulations of the apo form. Left: results from eight replicate simulations (1 μs each), with 7 Mg^{2+} ions placed initially by the MCTBI method. Right: results from four replicate simulations (1 μs each), with 16 Mg^{2+} ions placed initially by the Leap module.
(TIF)

S5 Fig. Distributions Mg^{2+} ions in simulations of the Q_1- and L_1-bound forms. Results using the ff99bsc0+χ_{OL3}/Li13 force field were from eight replicate simulations (1 μs each); those using the CUFIX/Li13 and ff99bsc0+χ_{OL3}/Allner12 force fields were from four replicate simulations (1 μs each).
(TIF)

S6 Fig. Loosening in the back of the binding pocket when bound with synthetic ligands. (A) Representative conformations of the Q_0-, L_2-, and L_{3M}-bound forms in cMD simulations with Mg^{2+}. Ligands are shown in both stick representation and as dot surface. The C1' atoms of C15 and C30 are connected to define the distance $d_{15\text{-}30}$. (B) The probability densities of $d_{15\text{-}30}$ in cMD simulations of the apo form and the five liganded forms without Mg^{2+}. (C) Representative conformations of the Q_1-, Q_0-, L_1-, L_2-, L_{3m}-, and L_{3M}-bound forms in cMD simulations with Mg^{2+}. The C1' atoms of G5 and G11 are connected to define the distance $d_{5\text{-}11}$. (D) The probability densities of $d_{5\text{-}11}$ in cMD simulations of the apo form and the five liganded forms with Mg^{2+}. (E) The probability densities of $d_{5\text{-}11}$ in cMD simulations of the apo form and the five liganded forms without Mg^{2+}. (F)-(H) Two views into Q_0, L_2, and L_{3m}, respectively, in the binding pocket. The aptamer is shown as gray surface while the ligands are shown as green spheres. The front and back views are shown on the left and right, respectively, in each panel.
(TIF)

S7 Fig. Unbinding and rebinding pathways of ligands. (A) The trajectories of ligand centers shown as dots colored according to the MD simulation time. The aptamer and bound ligands are shown in cartoon and stick representations, respectively. Top: Q_0; middle: L_1; and bottom: L_2. A plane in purple bisects the binding pocket into the front half and the back half. Two nucleotides defining the front door in the Q_0-bound complex are labeled in red; two nucleotides defining the back door in the L_1- and L_2-bound complexes are labeled in blue. (B) Time traces of r and z in three metadynamics simulations. Red dashed and green dotted horizontal lines are drawn at r = 1 and 9 Å, respectively, to indicate the times of entrance to and exit from the binding pocket.
(TIF)

S1 Movie. The cognate ligand Q_1 adopts a stable pose and forms stable hydrogen bonds inside the binding pocket. The methylamine head group samples alternative torsion angles.
(MP4)

S2 Movie. The synthetic ligand L_3 readily switches between two poses, hydrogen bonding with either A29 or U6.
(MP4)

S3 Movie. Cognate ligands (Q_1 shown) prefer to enter and exit through the front door between G5 and G11.
(MP4)

S4 Movie. Synthetic ligands (L_3 shown) prefer to enter and exit through the back door between C15 and C30.
(MP4)

Author Contributions

Conceptualization: Guodong Hu, Huan-Xiang Zhou.

Data curation: Guodong Hu.

Formal analysis: Guodong Hu.

Funding acquisition: Huan-Xiang Zhou.

Investigation: Guodong Hu, Huan-Xiang Zhou.

Methodology: Guodong Hu, Huan-Xiang Zhou.

Project administration: Huan-Xiang Zhou.

Software: Guodong Hu.

Supervision: Huan-Xiang Zhou.

Validation: Guodong Hu, Huan-Xiang Zhou.

Visualization: Guodong Hu, Huan-Xiang Zhou.

Writing – original draft: Guodong Hu, Huan-Xiang Zhou.

Writing – review & editing: Huan-Xiang Zhou.

References

1. Thomas JR, Hergenrother PJ. Targeting RNA with small molecules. Chem Rev. 2008; 108(4):1171–224. Epub 2008/03/26. https://doi.org/10.1021/cr0681546 PMID: 18361529.
2. Cech TR, Steitz JA. The noncoding RNA revolution-trashing old rules to forge new ones. Cell. 2014; 157(1):77–94. https://doi.org/10.1016/j.cell.2014.03.008 PMID: 24679528.
3. Guan L, Disney MD. Recent advances in developing small molecules targeting RNA. ACS Chem Biol. 2012; 7(1):73–86. https://doi.org/10.1021/cb200447r PMID: 22185671.
4. Connelly CM, Moon MH, Schneekloth JS Jr. The Emerging Role of RNA as a Therapeutic Target for Small Molecules. Cell Chem Biol. 2016; 23(9):1077–90. https://doi.org/10.1016/j.chembiol.2016.05.021 PMID: 27593111; PubMed Central PMCID: PMC5064864.
5. Sponer J, Bussi G, Krepl M, Banas P, Bottaro S, Cunha RA, et al. RNA Structural Dynamics As Captured by Molecular Simulations: A Comprehensive Overview. Chem Rev. 2018; 118(8):4177–338. https://doi.org/10.1021/acs.chemrev.7b00427 PMID: 29297679.
6. Palermo G, Casalino L, Magistrato A, Andrew McCammon J. Understanding the mechanistic basis of non-coding RNA through molecular dynamics simulations. J Struct Biol. 2019; 206(3):267–79. https://doi.org/10.1016/j.jsb.2019.03.004 PMID: 30880083; PubMed Central PMCID: PMC6637970.
7. Garst AD, Edwards AL, Batey RT. Riboswitches: structures and mechanisms. Cold Spring Harb Perspect Biol. 2011; 3(6):a003533. https://doi.org/10.1101/cshperspect.a003533 PMID: 20943759.
8. Sudarsan N, Wickiser JK, Nakamura S, Ebert MS, Breaker RR. An mRNA structure in bacteria that controls gene expression by binding lysine. Genes Dev. 2003; 17(21):2688–97. https://doi.org/10.1101/gad.1140003 PMID: 14597663; PubMed Central PMCID: PMC280618.
9. Mandal M, Boese B, Barrick JE, Winkler WC, Breaker RR. Riboswitches control fundamental biochemical pathways in Bacillus subtilis and other bacteria. Cell. 2003; 113(5):577–86. https://doi.org/10.1016/s0092-8674(03)00391-x PMID: 12787499.
10. Mandal M, Lee M, Barrick JE, Weinberg Z, Emilsson GM, Ruzzo WL, et al. A glycine-dependent riboswitch that uses cooperative binding to control gene expression. Science. 2004; 306(5694):275–9. https://doi.org/10.1126/science.1100829 PMID: 15472076.
11. Mandal M, Breaker RR. Adenine riboswitches and gene activation by disruption of a transcription terminator. Nat Struct Mol Biol. 2004; 11(1):29–35. https://doi.org/10.1038/nsmb710 PMID: 14718920.
12. Barrick JE, Breaker RR. The distributions, mechanisms, and structures of metabolite-binding riboswitches. Genome Biol. 2007; 8(11):R239. https://doi.org/10.1186/gb-2007-8-11-r239 PMID: 17997835; PubMed Central PMCID: PMC2258182.
13. Dann CE 3rd, Wakeman CA, Sieling CL, Baker SC Irnov I, Winkler WC. Structure and mechanism of a metal-sensing regulatory RNA. Cell. 2007; 130(5):878–92. https://doi.org/10.1016/j.cell.2007.06.051 PMID: 17803910.

14. Roth A, Breaker RR. The structural and functional diversity of metabolite-binding riboswitches. Annu Rev Biochem. 2009; 78:305–34. Epub 2009/03/21. https://doi.org/10.1146/annurev.biochem.78.070507.135656 PMID: 19298181; PubMed Central PMCID: PMC5325118.

15. Serganov A, Huang L, Patel DJ. Coenzyme recognition and gene regulation by a flavin mononucleotide riboswitch. Nature. 2009; 458(7235):233–7. https://doi.org/10.1038/nature07642 PMID: 19169240; PubMed Central PMCID: PMC3726715.

16. Kim JN, Blount KF, Puskarz I, Lim J, Link KH, Breaker RR. Design and antimicrobial action of purine analogues that bind Guanine riboswitches. ACS Chem Biol. 2009; 4(11):915–27. Epub 2009/09/11. https://doi.org/10.1021/cb900146k PMID: 19739679; PubMed Central PMCID: PMC4140397.

17. Priyakumar UD, MacKerell AD Jr. Role of the adenine ligand on the stabilization of the secondary and tertiary interactions in the adenine riboswitch. J Mol Biol. 2010; 396(5):1422–38. https://doi.org/10.1016/j.jmb.2009.12.024 PMID: 20026131; PubMed Central PMCID: PMC2824916.

18. Daldrop P, Reyes FE, Robinson DA, Hammond CM, Lilley DM, Batey RT, et al. Novel ligands for a purine riboswitch discovered by RNA-ligand docking. Chem Biol. 2011; 18(3):324–35. Epub 2011/03/29. S1074-5521(11)00039-1 [pii] https://doi.org/10.1016/j.chembiol.2010.12.020 PMID: 21439477; PubMed Central PMCID: PMC3119931.

19. Deigan KE, Ferre-D'Amare AR. Riboswitches: discovery of drugs that target bacterial gene-regulatory RNAs. Acc Chem Res. 2011; 44(12):1329–38. https://doi.org/10.1021/ar200039b PMID: 21615107; PubMed Central PMCID: PMC3193592.

20. Warner KD, Homan P, Weeks KM, Smith AG, Abell C, Ferre-D'Amare AR. Validating fragment-based drug discovery for biological RNAs: lead fragments bind and remodel the TPP riboswitch specifically. Chem Biol. 2014; 21(5):591–5. Epub 2014/04/29. S1074-5521(14)00113-6 [pii] https://doi.org/10.1016/j.chembiol.2014.03.007 PMID: 24768306; PubMed Central PMCID: PMC4057041.

21. Howe JA, Wang H, Fischmann TO, Balibar CJ, Xiao L, Galgoci AM, et al. Selective small-molecule inhibition of an RNA structural element. Nature. 2015; 526(7575):672–7. https://doi.org/10.1038/nature15542 PMID: 26416753.

22. Sund J, Lind C, Aqvist J. Binding site preorganization and ligand discrimination in the purine riboswitch. The journal of physical chemistry B. 2015; 119(3):773–82. https://doi.org/10.1021/jp5052358 PMID: 25014157.

23. Connelly CM, Numata T, Boer RE, Moon MH, Sinniah RS, Barchi JJ, et al. Synthetic ligands for PreQ1 riboswitches provide structural and mechanistic insights into targeting RNA tertiary structure. Nat Commun. 2019; 10(1):1501. https://doi.org/10.1038/s41467-019-09493-3 PMID: 30940810; PubMed Central PMCID: PMC6445138.

24. Jenkins JL, Krucinska J, McCarty RM, Bandarian V, Wedekind JE. Comparison of a preQ1 riboswitch aptamer in metabolite-bound and free states with implications for gene regulation. J Biol Chem. 2011; 286(28):24626–37. https://doi.org/10.1074/jbc.M111.230375 PMID: 21592962; PubMed Central PMCID: PMC3137038.

25. Schroeder GM, Dutta D, Cavender CE, Jenkins JL, Pritchett EM, Baker CD, et al. Analysis of a preQ1-I riboswitch in effector-free and bound states reveals a metabolite-programmed nucleobase-stacking spine that controls gene regulation. Nucleic Acids Res. 2020; 48(14):8146–64. https://doi.org/10.1093/nar/gkaa546 PMID: 32597951.

26. Spitale RC, Torelli AT, Krucinska J, Bandarian V, Wedekind JE. The structural basis for recognition of the PreQ0 metabolite by an unusually small riboswitch aptamer domain. J Biol Chem. 2009; 284(17):11012–6. https://doi.org/10.1074/jbc.C900024200 PMID: 19261617; PubMed Central PMCID: PMC2670106.

27. Allner O, Nilsson L, Villa A. Loop-loop interaction in an adenine-sensing riboswitch: a molecular dynamics study. RNA. 2013; 19(7):916–26. https://doi.org/10.1261/rna.037549.112 PMID: 23716711; PubMed Central PMCID: PMC3683926.

28. Di Palma F, Colizzi F, Bussi G. Ligand-induced stabilization of the aptamer terminal helix in the add adenine riboswitch. RNA. 2013; 19(11):1517–24. https://doi.org/10.1261/rna.040493.113 PMID: 24051105; PubMed Central PMCID: PMC3851719.

29. Hu G, Ma A, Wang J. Ligand Selectivity Mechanism and Conformational Changes in Guanine Riboswitch by Molecular Dynamics Simulations and Free Energy Calculations. J Chem Inf Model. 2017; 57(4):918–28. https://doi.org/10.1021/acs.jcim.7b00139 PMID: 28345904.

30. Chen J, Wang X, Pang L, Zhang JZH, Zhu T. Effect of mutations on binding of ligands to guanine riboswitch probed by free energy perturbation and molecular dynamics simulations. Nucleic Acids Res. 2019; 47(13):6618–31. https://doi.org/10.1093/nar/gkz499 PMID: 31173143; PubMed Central PMCID: PMC6649850.

31. Petrone PM, Dewhurst J, Tommasi R, Whitehead L, Pomerantz AK. Atomic-scale characterization of conformational changes in the preQ(1) riboswitch aptamer upon ligand binding. J Mol Graph Model.

2011; 30:179–85. Epub 2011/08/13. S1093-3263(11)00108-2 [pii] https://doi.org/10.1016/j.jmgm.2011.07.006 PMID: 21831681.

32. Yoon J, Thirumalai D, Hyeon C. Urea-Induced Denaturation of PreQ(1)-Riboswitch. J Am Chem Soc. 2013; 135(32):12112–21. https://doi.org/10.1021/ja406019s WOS:238631261200067.

33. Gong Z, Zhao Y, Chen C, Duan Y, Xiao Y. Insights into ligand binding to PreQ1 Riboswitch Aptamer from molecular dynamics simulations. Plos One. 2014; 9(3):e92247. Epub 2014/03/26. https://doi.org/10.1371/journal.pone.0092247 PONE-D-13-44748 [pii]. PMID: 24663240; PubMed Central PMCID: PMC3963873.

34. Wang C, Greene D, Xiao L, Qi R, Luo R. Recent Developments and Applications of the MMPBSA Method. Front Mol Biosci. 2017; 4:87. https://doi.org/10.3389/fmolb.2017.00087 PMID: 29367919; PubMed Central PMCID: PMC5768160.

35. Yuan X, Raniolo S, Limongelli V, Xu Y. The Molecular Mechanism Underlying Ligand Binding to the Membrane-Embedded Site of a G-Protein-Coupled Receptor. Journal of chemical theory and computation. 2018; 14(5):2761–70. https://doi.org/10.1021/acs.jctc.8b00046 PMID: 29660291.

36. Limongelli V, Marinelli L, Cosconati S, La Motta C, Sartini S, Mugnaini L, et al. Sampling protein motion and solvent effect during ligand binding. Proc Natl Acad Sci U S A. 2012; 109(5):1467–72. Epub 2012/01/13. 1112181108 [pii] https://doi.org/10.1073/pnas.1112181108 PMID: 22238423; PubMed Central PMCID: PMC3277130.

37. Shang Y, Yeatman HR, Provasi D, Alt A, Christopoulos A, Canals M, et al. Proposed Mode of Binding and Action of Positive Allosteric Modulators at Opioid Receptors. ACS Chem Biol. 2016; 11(5):1220–9. Epub 2016/02/04. https://doi.org/10.1021/acschembio.5b00712 PMID: 26841170; PubMed Central PMCID: PMC4950826.

38. Hu G, Yu X, Bian Y, Cao Z, Xu S, Zhao L, et al. Atomistic Analysis of ToxN and ToxI Complex Unbinding Mechanism. Int J Mol Sci. 2018; 19(11):3523. https://doi.org/10.3390/ijms19113524 PMID: 30423909.

39. Di Leva FS, Novellino E, Cavalli A, Parrinello M, Limongelli V. Mechanistic insight into ligand binding to G-quadruplex DNA. Nucleic Acids Res. 2014; 42(9):5447–55. https://doi.org/10.1093/nar/gku247 PMID: 24753420; PubMed Central PMCID: PMC4027208.

40. Barducci A, Bussi G, Parrinello M. Well-tempered metadynamics: a smoothly converging and tunable free-energy method. Phys Rev Lett. 2008; 100(2):020603. https://doi.org/10.1103/PhysRevLett.100.020603 PMID: 18232845.

41. Draper DE. A guide to ions and RNA structure. RNA. 2004; 10(3):335–43. https://doi.org/10.1261/rna.5205404 PMID: 14970378; PubMed Central PMCID: PMC1370927.

42. Fischer NM, Poleto MD, Steuer J, van der Spoel D. Influence of Na+ and Mg2+ ions on RNA structures studied with molecular dynamics simulations. Nucleic Acids Res. 2018; 46(10):4872–82. https://doi.org/10.1093/nar/gky221 PMID: 29718375; PubMed Central PMCID: PMC6007214.

43. Bao L, Wang J, Xiao Y. Dynamics of metal ions around an RNA molecule. Phys Rev E. 2019; 99(1):012420. https://doi.org/10.1103/PhysRevE.99.012420 WOS:307803360900003.

44. Misra VK, Draper DE. A thermodynamic framework for Mg2+ binding to RNA. Proc Natl Acad Sci U S A. 2001; 98(22):12456–61. https://doi.org/10.1073/pnas.221234598 PMID: 11675490; PubMed Central PMCID: PMC60075.

45. Bowman JC, Lenz TK, Hud NV, Williams LD. Cations in charge: magnesium ions in RNA folding and catalysis. Curr Opin Struct Biol. 2012; 22(3):262–72. https://doi.org/10.1016/j.sbi.2012.04.006 PMID: 22595008.

46. Suddala KC, Wang J, Hou Q, Walter NG. Mg(2+) shifts ligand-mediated folding of a riboswitch from induced-fit to conformational selection. J Am Chem Soc. 2015; 137(44):14075–83. Epub 2015/10/17. https://doi.org/10.1021/jacs.5b09740 PMID: 26471732; PubMed Central PMCID: PMC5098500.

47. Nayal M, Di Cera E. Valence screening of water in protein crystals reveals potential Na+ binding sites. J Mol Biol. 1996; 256(2):228–34. https://doi.org/10.1006/jmbi.1996.0081 PMID: 8594192

48. Hayes RL, Noel JK, Mohanty U, Whitford PC, Hennelly SP, Onuchic JN, et al. Magnesium fluctuations modulate RNA dynamics in the SAM-I riboswitch. J Am Chem Soc. 2012; 134(29):12043–53. Epub 2012/05/23. https://doi.org/10.1021/ja301454u PMID: 22612276; PubMed Central PMCID: PMC3675279.

49. Lin YF, Cheng CW, Shih CS, Hwang JK, Yu CS, Lu CH. MIB: Metal Ion-Binding Site Prediction and Docking Server. J Chem Inf Model. 2016; 56(12):2287–91. https://doi.org/10.1021/acs.jcim.6b00407 PMID: 27976886.

50. Hu X, Dong Q, Yang J, Zhang Y. Recognizing metal and acid radical ion-binding sites by integrating ab initio modeling with template-based transferals. Bioinformatics. 2016; 32(21):3260–9. https://doi.org/10.1093/bioinformatics/btw396 PMID: 27378301; PubMed Central PMCID: PMC5079472.

51. Philips A, Milanowska K, Lach G, Boniecki M, Rother K, Bujnicki JM. MetalionRNA: computational predictor of metal-binding sites in RNA structures. Bioinformatics. 2012; 28(2):198–205. https://doi.org/10.1093/bioinformatics/btr636 PMID: 22110243; PubMed Central PMCID: PMC3259437.

52. Sun LZ, Chen SJ. Monte Carlo Tightly Bound Ion Model: Predicting Ion-Binding Properties of RNA with Ion Correlations and Fluctuations. Journal of chemical theory and computation. 2016; 12(7):3370–81. https://doi.org/10.1021/acs.jctc.6b00028 PMID: 27311366; PubMed Central PMCID: PMC5520805.

53. Sun LZ, Zhang JX, Chen SJ. MCTBI: a web server for predicting metal ion effects in RNA structures. RNA. 2017; 23(8):1155–65. https://doi.org/10.1261/rna.060947.117 PMID: 28450533; PubMed Central PMCID: PMC5513060.

54. Cheatham TE, Cieplak P, Kollman PA. A Modified Version of the Cornell et al. Force Field with Improved Sugar Pucker Phases and Helical Repeat. J Biomol Struct Dyn. 1999; 16(4):845–62. https://doi.org/10.1080/07391102.1999.10508297 PMID: 10217454

55. Perez A, Marchan I, Svozil D, Sponer J, Cheatham TE 3rd, Laughton CA, et al. Refinement of the AMBER force field for nucleic acids: improving the description of alpha/gamma conformers. Biophysical journal. 2007; 92(11):3817–29. https://doi.org/10.1529/biophysj.106.097782 PMID: 17351000; PubMed Central PMCID: PMC1868997.

56. Zgarbova M, Otyepka M, Sponer J, Mladek A, Banas P, Cheatham TE 3rd, et al. Refinement of the Cornell et al. Nucleic Acids Force Field Based on Reference Quantum Chemical Calculations of Glycosidic Torsion Profiles. Journal of chemical theory and computation. 2011; 7(9):2886–902. https://doi.org/10.1021/ct200162x PMID: 21921995; PubMed Central PMCID: PMC3171997.

57. Li P, Roberts BP, Chakravorty DK, Merz KM Jr. Rational Design of Particle Mesh Ewald Compatible Lennard-Jones Parameters for +2 Metal Cations in Explicit Solvent. Journal of chemical theory and computation. 2013; 9(6):2733–48. https://doi.org/10.1021/ct400146w PMID: 23914143; PubMed Central PMCID: PMC3728907.

58. Yoo J, Aksimentiev A. Improved Parameterization of Amine–Carboxylate and Amine–Phosphate Interactions for Molecular Dynamics Simulations Using the CHARMM and AMBER Force Fields. Journal of chemical theory and computation. 2016; 12(1):430–43. https://doi.org/10.1021/acs.jctc.5b00967 PMID: 26632962

59. Allnér O, Nilsson L, Villa A. Magnesium Ion–Water Coordination and Exchange in Biomolecular Simulations. Journal of chemical theory and computation. 2012; 8(4):1493–502. https://doi.org/10.1021/ct3000734 PMID: 26596759

60. Gohlke H, Kiel C, Case DA. Insights into protein–protein binding by binding free energy calculation and free energy decomposition for the Ras–Raf and Ras–RalGDS complexes. J Mol Biol. 2003; 330(4):891–913. https://doi.org/10.1016/s0022-2836(03)00610-7 PMID: 12850155

61. Hu G, Wang J. Ligand selectivity of estrogen receptors by a molecular dynamics study. Eur J Med Chem. 2014; 74:726–35. https://doi.org/10.1016/j.ejmech.2013.04.049 PMID: 23694906

62. Wang E, Sun H, Wang J, Wang Z, Liu H, Zhang JZH, et al. End-Point Binding Free Energy Calculation with MM/PBSA and MM/GBSA: Strategies and Applications in Drug Design. Chem Rev. 2019; 119(16):9478–508. Epub 2019/06/28. https://doi.org/10.1021/acs.chemrev.9b00055 PMID: 31244000.

63. Case DA, Ben-Shalom IY, Brozell SR, Cerutti DS, III TEC, Cruzeiro VWD, et al. Amber 18: University of California: San Francisco; 2018.

64. Börjesson K, Preus S, El-Sagheer AH, Brown T, Albinsson B, Wilhelmsson LM. Nucleic Acid Base Analog FRET-Pair Facilitating Detailed Structural Measurements in Nucleic Acid Containing Systems. J Am Chem Soc. 2009; 131(12):4288–93. https://doi.org/10.1021/ja806944w PMID: 19317504

65. Frisch MJ, Trucks GW, Schlegel HB, Scuseria GE, Robb MA, Cheeseman JR, et al. Gaussian 16 Rev. C.01. Wallingford, CT 2016.

66. Jorgensen WL, Chandrasekhar J, Madura JD, Impey RW, Klein ML. Comparison of simple potential functions for simulating liquid water. J Comput Phys. 1983; 79:926–35.

67. Wang J, Wolf RM, Caldwell JW, Kollman PA, Case DA. Development and testing of a general amber force field. J Comput Chem. 2004; 25(9):1157–74. https://doi.org/10.1002/jcc.20035 PMID: 15116359.

68. Joung IS, Cheatham TE 3rd. Determination of alkali and halide monovalent ion parameters for use in explicitly solvated biomolecular simulations. The journal of physical chemistry B. 2008; 112(30):9020–41. https://doi.org/10.1021/jp8001614 PMID: 18593145; PubMed Central PMCID: PMC2652252.

69. Pastor RW, Brooks BR, Szabo A. An Analysis of the Accuracy of Langevin and Molecular Dynamics Algorithms. Mol Phys. 1988; 65(6):1409–19. https://doi.org/10.1080/00268978800101881 WOS: A1988T130200011.

70. Berendsen HJC, Postma JPM, Gunsteren WFv, DiNola A, Haak JR. Molecular dynamics with coupling to an external bath. J Chem Phys. 1984; 81(8):3684–90. https://doi.org/10.1063/1.448118

71. Ryckaert JP, Ciccotti G, Berendsen HJC. Numerical-integration of cartesian equations of motion of a system with constraints—molecular-dynamics of N-Alkanes. J Comput Phys. 1977; 23:327–41.

72. Darden T, York D, Pedersen L. Particle mesh Ewald: an N.Log(N) method for Ewald sums in large systems. J Comput Phys. 1993; 98:10089–92.

73. Onufriev A, Bashford D, Case DA. Exploring protein native states and large-scale conformational changes with a modified generalized born model. Proteins. 2004; 55(2):383–94. https://doi.org/10.1002/prot.20033 PMID: 15048829.

74. Sitkoff D, Sharp KA, Honig B. Accurate Calculation of Hydration Free Energies Using Macroscopic Solvent Models. J Phys Chem. 1994; 98(7):1978–88. https://doi.org/10.1021/j100058a043

75. Humphrey W, Dalke A, Schulten K. VMD: Visual molecular dynamics. J Mol Graph. 1996; 14(1):33–8. https://doi.org/10.1016/0263-7855(96)00018-5 PMID: 8744570

76. Roe DR, Cheatham TE. PTRAJ and CPPTRAJ: Software for Processing and Analysis of Molecular Dynamics Trajectory Data. Journal of chemical theory and computation. 2013; 9:3084–95. https://doi.org/10.1021/ct400341p PMID: 26583988

77. Romo TD, Leioatts N, Grossfield A. Lightweight object oriented structure analysis: tools for building tools to analyze molecular dynamics simulations. J Comput Chem. 2014; 35(32):2305–18. https://doi.org/10.1002/jcc.23753 PMID: 25327784; PubMed Central PMCID: PMC4227929.

78. Tribello GA, Bonomi M, Branduardi D, Camilloni C, Bussi G. Plumed 2: New feathers for an old bird. Comput Phys Commun. 2014; 185(2):604–13.

79. Abraham MJ, Spoel Dvd, Lindahl E, Hess B, team Gd. GROMACS User Manual version 5.1.2. www.gromacs.org2016.